NASA Contractor Report 194967

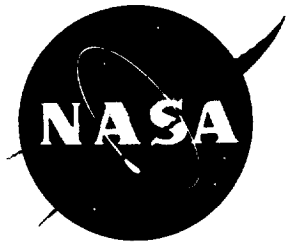

An Implementation of a Chemical and Thermal Nonequilibrium Flow Solver on Unstructured Meshes and Application to Blunt Bodies

Ramadas K. Prabhu
Lockheed Engineering & Sciences Company, Hampton, VA

Contract NAS1-19000

August 1994

National Aeronautics and Space Administration
Langley Research Center
Hampton, Virginia 23681-0001

FOREWORD

This document was prepared by Lockheed Engineering & Sciences Company, Langley Program Office, for the National Aeronautics and Space Administration, Langley Research Center, Hampton, Virginia. The work reported was performed under contract NAS1-19000. Dr. Allan R. Wieting was the NASA Technical Monitor for this task.

SUMMARY

This paper presents a nonequilibrium flow solver, implementation of the algorithm on unstructured meshes, and application to hypersonic flow past a blunt bodies. Air is modeled as a mixture of five chemical species, namely O2, N2, O, NO, and N, and having two temperatures, namely translational and vibrational. The solution algorithm is a cell-centered, point-implicit upwind scheme that employs Roe's flux difference splitting technique. Implementation of this algorithm on unstructured meshes is described. The computer code is applied to solve Mach 15 flow with and without a Type IV shock interference on a cylindrical body of 2.54 mm (0.1 inch) radius representing a cowl lip. Adaptively generated unstructured meshes are employed, and the meshes are refined several times until the solution exhibits detailed flow features and surface pressure and heat flux distributions. Effects of a catalytic wall on surface heat flux distribution are studied. For the Mach 15 Type IV shock interference flow, present results showed a peak heat flux of 544 MW/m^2 for a fully catalytic wall and 431 MW/m^2 for a noncatalytic wall. Some of the results are compared with available computational data.

INTRODUCTION

The study of hypersonic flows has gained momentum with the advent of concepts like the National AeroSpace Plane (NASP) and similar transatmospheric vehicles. Under the very high velocity and temperature conditions experienced by hypersonic vehicles, departure from chemical and thermal equilibrium occurs. Properties of air change dramatically as new chemical species are produced at the expense of others. The simple one temperature model used to describe the energy of air becomes inapplicable, and it becomes necessary to consider one or more additional temperatures (corresponding to vibrational and electronic energies). Determination of aerothermal loads on blunt bodies in such an environment is of great importance, and forms the subject of the present study.

In high speed flows, any adjustment of chemical composition or thermodynamic equilibrium to a change in local environment requires certain time. This is because the redistribution of chemical species and internal energies require certain number of molecular collisions, and hence a certain characteristic time. Chemical nonequilibrium occurs when the characteristic time for the chemical reactions to reach local equilibrium is of the same order as the as the characteristic time of the fluid flow. Similarly, thermal nonequilibrium occurs when the characteristic time for translational and various internal energy modes to reach local equilibrium is of the same order as the as the characteristic time of the fluid flow. Since the chemical and thermal changes are the results of collisions between the constituent particles, nonequilibrium effects prevail in high-speed flows in low-density air.

In chemical nonequilibrium flows the mass conservation equation is applied to each of the constituent species in the gas mixture. Therefore, the overall mass conservation equation is replaced by as many species conservation equations as the number of chemical species considered. The assumption of thermal nonequilibrium introduces additional energy conservation equations - one for every additional energy mode. Thus, the number of governing equations for nonequilibrium flow is much bigger compared to those for perfect gas flow. A complete set of governing equations for nonequilibrium flow may be found in Gnoffo, et al. (Ref. 1) and Lee (Ref. 2).

Analysis of nonequilibrium flow is rather complex because (1) the number of equations to be solved is much larger than the Navier-Stokes equations, and (2) there are additional terms like the species production, mass diffusion, and vibrational energy relaxation, etc., that appear in the governing equations. In a typical flight of the NASP flying at Mach 15, ionization is not expected to occur, and a 5-species air is adequate for the analysis (see Gupta, et al, Fig. 1, Ref. 3). Since the rotational characteristic temperatures for the constituent species (namely O2, N2, O, NO, and N) are small, the translational and rotational energy modes are assumed to be in equilibrium, whereas the vibrational energy mode is assumed to be in nonequilibrium. We have simplified the thermodynamic model by assuming a harmonic oscillator to describe the vibrational energy. Ionic species and electrons are not considered. This simplifies the set of governing equations by eliminating the equation governing electron and electronic excitation energy. In the present analysis, we have taken the complete set of governing equations from Gnoffo, et al. (Ref. 1), and simplified them for a five-species two-temperature air model.

A cell-centered, point-implicit, upwind scheme using Roe's flux difference splitting tech-

nique is employed for the inviscid terms of the governing equations. An existing set of computer codes, Langley Adaptive Remeshing Code and NaviEr Stokes Solver (LARCNESS, see Ref. 4), is modified for nonequilibrium flow of air with five chemical species, namely O2, N2, O, NO, and N, and two temperatures, namely translational-rotational and vibrational temperatures. The solver is first-order accurate in space and time. Adaptively generated unstructured meshes consisting of triangular and quadrilateral elements are employed to discretize the computational domain; the adaptive remeshing strategy places small elements in regions of large second derivatives of selected flow variables, and facilitates effective capturing of sharp flow features.

When an oblique shock wave impinges on a bow shock in front of a blunt body like the leading edge of an engine cowl, a complex flow pattern results. Edney (Ref. 5) studied these flow patterns extensively, and classified them into six types. Of these, the Type IV shock interference (see Fig. 1), is characterized by two triple points, two shear layers, and a supersonic jet (in between the shear layers) that undergoes repeated compressions and expansions before impinging on the body. Impingement of this supersonic jet causes intense heating at the stagnation point. The knowledge of thermal loads forms an important input in the design of such leading edges.

In the present paper a Type IV shock interference in Mach 15 flow past a blunt body of 2.54 mm radius is solved. This body is typical of the engine cowl lip of the NASP. The effects of a catalytic wall on the heat flux distribution on the wall are studied. The results are compared with other numerical results.

Symbols:

$\bar{a}_{i,j}$	constants that appear in computing thermal conductivity
$a_{i,j}$	constants that appear in the curve fits for $c_{p,t,i}$
A	Avogadro constant, 6.022 045 E+23 per mol
c_i	average speed of molecules of species i, m/s
c	speed of sound, m/s
c_f	$= f/\rho_\infty u_\infty^2$, skin friction coefficient
$c_{p,t,i}$	specific heat at constant pressure per mole of species i for translational energy, J/mol-K

$c_{v,r,i}$	specific heat at constant volume per mole of species i for rotational energy, J/mol-K
$c_{v,t,i}$	specific heat at constant volume per mole of species i for translational energy, J/mol-K
$c_{v,v,i}$	specific heat at constant volume per mole of species i for vibrational energy, J/mol-K
D_i	effective diffusion coefficient for species i
$\widehat{D}_i$	average vibrational energy of molecule i, that is created or destroyed, J/kg
d	distance from the body surface in radial direction, (negative outwards), m
E	$= e + (u^2 + v^2)/2$, total energy (sum of internal and kinetic energies) per unit mass of gas mixture, J/kg
e	$= e_t + e_r + e_v$, internal energy per unit mass of the mixture, J/kg
e_r	rotational energy per unit mass of the gas mixture, J/kg
e_t	translational energy per unit mass of the gas mixture, J/kg
e_v	vibrational energy per unit mass of the gas mixture, J/kg
$e_{r,i}$	rotational energy per mole of species i, J/mol
$e_{t,i}$	translational energy per mole of species i, J/mol
$e_{v,i}$	vibrational energy per mole of species i, J/mol
$e^*_{v,i}$	vibrational energy at translational temperature per mole of species i, J/mol
f	skin friction, N
G_i	Gibbs energy for species i, J/mol-K
H	$= E + P/\rho$, enthalpy of the gas mixture, J/kg
h_i	enthalpy per mole of species i, J/mol
k	Boltzmann constant, 1.380 622 E-23 J/K
$k_{f,i}$, $k_{b,i}$	forward and backward reaction rate constants for reaction j
M	molecular weight of the mixture, kg/mol

M_i	molecular weight of species i, kg/mol
$m_{i,j}$	reduced molecular weights of species i and j
n_i	number density of species i, per mol
P	pressure, N/m^2
P_{t2}	pitot pressure in perfect gas, N/m^2
q	surface heat flux, MW/m^2, also
	$=(u^2 + v^2)/2$, dynamic pressure, N/m^2
R	universal gas constant, 8.314 J/mol-K
S	entropy of the gas mixture, J/kg-K
s_i	entropy of species i, J/mol-K
T	translational temperature, K
T_v	vibrational temperature, K
T_w	wall temperature, K
T_∞	freestream temperature, K
u, v	velocity components in x- and y-directions, m/s
u_∞	freestream velocity, m/s
x_i	mass fraction of species i
$\dot{w}_i$	rate of production of species i, kg/m^3-s.
Y_i	mole fraction of species i
α_i	$\frac{\partial P}{\partial \rho_i}$
β	$\frac{\partial P}{\partial (\rho E)}$
$\Delta_{i,j}^{(1)}, \Delta_{i,j}^{(2)}$	modified collision integrals for species i and j, m-s
$\Delta h_{f,i}$	heat of formation per mole of species i, J/mol
η_t	thermal conductivity for translational energy, J/m-s-K
η_r	thermal conductivity for rotational energy, J/m-s-K
η_v	thermal conductivity for vibrational energy, J/m-s-K

ρ	density, kg/m^3
ρ_i	partial density of species i, kg/m^3
μ	viscosity of the gas mixture, N-s/m^2
θ	angular location on the body, deg. (see Fig. 2)
$\Theta_{v,i}$	characteristic vibrational temperature of species i, K
σ	number of moles of the mixture per unit mass of the gas mixture, mol/kg
σ_i	number of moles of species i per unit mass of the mixture, mol/kg
τ_{xx}, τ_{xy}, τ_{yy}	viscous stresses, N/m^2
τ_i^M, τ_i^P	translational-vibrational relaxation times for molecular species, s
Ω_i	effective collision cross-section for vibrational relaxation, m^2
$\Omega_{i,j}^{(1,1)}$, $\Omega_{i,j}^{(2,2)}$	collision integrals for species i and j, m^2

Subscripts:

w	wall quantity
∞	Freestream value
i, j	indices for chemical species
r	rotational mode
t	translational mode
v	vibrational mode

GOVERNING EQUATIONS

The governing equations for two-dimensional flow in chemical and thermal nonequilibrium written in conservation form are as follows:

Species Conservation:

$$\frac{\partial \rho_i}{\partial t} + \frac{\partial \rho_i u}{\partial x} + \frac{\partial \rho_i v}{\partial y} = \dot{w}_i + \frac{\partial}{\partial x}\left(\rho D_i \frac{\partial Y_i}{\partial x}\right) + \frac{\partial}{\partial y}\left(\rho D_i \frac{\partial Y_i}{\partial y}\right) \tag{1}$$

Momentum Conservation:

$$\begin{aligned}\frac{\partial \rho u}{\partial t} + \frac{\partial (P + \rho u^2)}{\partial x} + \frac{\partial \rho uv}{\partial y} &= \frac{\partial}{\partial x}(\tau_{xx}) + \frac{\partial}{\partial y}(\tau_{xy}) \\ \frac{\partial \rho v}{\partial t} + \frac{\partial \rho uv}{\partial x} + \frac{\partial (P + \rho v^2)}{\partial y} &= \frac{\partial}{\partial x}(\tau_{xy}) + \frac{\partial}{\partial y}(\tau_{yy})\end{aligned} \tag{2}$$

Total Energy Conservation:

$$\begin{aligned}\frac{\partial \rho E}{\partial t} + \frac{\partial \rho Hu}{\partial x} + \frac{\partial \rho Hv}{\partial y} &= \frac{\partial}{\partial x}(u\tau_{xx} + v\tau_{xy}) + \frac{\partial}{\partial y}(u\tau_{xy} + v\tau_{yy}) \\ &+ \frac{\partial}{\partial x}\left(\eta_t \frac{\partial T}{\partial x} + \eta_v \frac{\partial T_v}{\partial x}\right) + \frac{\partial}{\partial y}\left(\eta_t \frac{\partial T}{\partial y} + \eta_v \frac{\partial T_v}{\partial y}\right) \\ &+ \frac{\partial}{\partial x}\left(\rho \sum_{i=1}^{5} \frac{h_i D_i}{W_i} \frac{\partial Y_i}{\partial x}\right) + \frac{\partial}{\partial y}\left(\rho \sum_{i=1}^{5} \frac{h_i D_i}{W_i} \frac{\partial Y_i}{\partial y}\right)\end{aligned} \tag{3}$$

Vibrational Energy Conservation:

$$\begin{aligned}\frac{\partial \rho e_v}{\partial t} + \frac{\partial \rho e_v u}{\partial x} + \frac{\partial \rho e_v v}{\partial y} &= \frac{\partial}{\partial x}\left(\eta_v \frac{\partial T_v}{\partial x}\right) + \frac{\partial}{\partial y}\left(\eta_v \frac{\partial T_v}{\partial y}\right) \\ &+ \frac{\partial}{\partial x}\left(\rho \sum_{i=mol} \frac{h_{v,i} D_i}{W_i} \frac{\partial Y_i}{\partial x}\right) + \frac{\partial}{\partial y}\left(\rho \sum_{i=mol} \frac{h_{v,i} D_i}{W_i} \frac{\partial Y_i}{\partial y}\right) \\ &+ \sum_{i=mol} \frac{\rho_i}{W_i}(e^*_{v,i} - e_{v,i})/\tau_i + \sum_{i=mol} \dot{w}_i \hat{D}_i\end{aligned} \tag{4}$$

These equations are simplified form of a complete set of governing equations given in Ref. 1, with minor changes in notation. A detailed description of each of the terms in these equations may be found in Ref. 1.

The reacting gas mixture is assumed to consist of five species, namely O_2, N_2, O, NO, and N; hence there are five components in Eqn. (1) -- one for each species. The density, ρ, of the gas mixture is the sum of the partial densities of the five species, i.e.,

$$\rho = \sum_{i=1}^{5} \rho_i \tag{5}$$

The species production terms, $\dot{w}_i$, $i = 1, \ldots, 5$, are in general, non-zero; however, the sum $\sum \dot{w}_i = 0$. Therefore, if the diffusion terms are neglected, and all the species conservation equations represented by Eqn. (1) are added, then we obtain the familiar overall mass conservation equation.

The gas mixture is assumed to behave as a perfect gas; hence the pressure, P, is given by

the equation for a thermally perfect gas, i.e.,

$$P = \rho RT\sum_{i=1}^{5}\sigma_i = \rho RT\sigma \tag{6}$$

where $\sigma = \sum\sigma_i$, and $\sigma_i, i = 1, \ldots, 5$ are the mole numbers of the species i per unit mass of the mixture. Note that the molecular weight of the gas mixture, M, is equal to $1/\sigma$. The value of the universal gas constant, R, is 8.314 J/mol-K. The above equation can also be written as follows:

$$P = TR\sum_{i=1}^{5}\rho_i/M_i \tag{7}$$

where $M_i, i = 1, \ldots, 5$ are the molecular weights of species i.

THERMODYNAMIC MODEL

The total energy, E, is the sum of the internal energy and the kinetic energy. The internal energy is the sum of translational energy, e_t, rotational energy, e_r, and vibrational energy, e_v. These energies are given by the following relations:

$$\begin{aligned} e_t &= \sum_{i=1}^{5} e_{t,i}\sigma_i = \sum_{i=1}^{5}\left(\int_0^T c_{v,t,i}(T')\,dT' + \Delta h_{f,i}\right)\sigma_i \\ e_r &= \sum_{i=1}^{5} e_{r,i}\sigma_i = \sum_{i=1}^{5}\sigma_i\int_0^T c_{v,r,i}(T')\,dT' \\ e_v &= \sum_{i=1}^{5} e_{v,i}\sigma_i = \sum_{i=1}^{5}\sigma_i\int_0^{T_v} c_{v,v,i}(T')\,dT' \end{aligned} \tag{8}$$

The reference temperature is taken as zero Kelvin. The heat of formation, $\Delta h_{f,i}$ for O_2 and N_2 are zero. The values of $\Delta h_{f,i}$ for O, NO, and N at the reference temperature taken from Prabhu and Erickson (Ref. 6) are 246,783 J/mol, 90,671 J/mol, and 470,816 J/mol, respectively. The heat capacities for the three energy modes are given by the following relations:

$$\begin{aligned} c_{v,t,i}(T) &= 2.5R \\ c_{v,r,i}(T) &= R \\ c_{v,v,i}(T_v) &= R\frac{exp\,(\Theta_{v,i}/T_v)}{[exp\,(\Theta_{v,i}/T_v) - 1]^2}\left(\frac{\Theta_{v,i}}{T_v}\right)^2 \end{aligned} \tag{9}$$

Note that the translational and rotational energy modes are assumed to be fully excited, and hence the heat capacities for these modes are independent of temperature. The vibrational energy mode

is assumed to be not fully excited, and hence the vibrational heat capacity is a function of the vibrational temperature. The above expression for $c_{v,v,i}$ is from Vincenti and Kruger (Ref. 7), and is the result of the assumption that the molecules may be regarded as harmonic oscillators. The characteristic temperature for vibration, $\Theta_{v,i}$ appearing in Eqn. (9) is 2,270 K for O_2, 3,390 K for N_2, and 2,740 K for NO. Note that when the vibrational energy mode becomes fully excited, i.e., when $T_v >> \Theta_{v,i}$, $c_{v,v,i} = R$.

The total enthalpy is given by

$$H = E + P/\rho \tag{10}$$

In the present computational scheme, the partial derivatives of pressure with respect to the conserved variables are required. These derivatives are evaluated as follows.

First, the equation of state given by Eqn. (6) is rewritten as follow:

$$P = T\Sigma R_i \rho_i \tag{11}$$

Note that $R_i = R/M_i$. Equation (11) may be written in differential form as

$$dP = R\Sigma(\rho_i/M_i)\,dT + T\Sigma R_i d\rho_i \tag{12}$$

Next, an expression for dT can be derived from the definition of total energy, and is given by

$$dT = \left[d(\rho E) - Ed\rho - de_v + e_v d\rho - \Sigma e_{t,i}(d\rho_i - x_i d\rho)/M_i + (u^2+v^2)\,d\rho + ud\rho u + vd\rho v\right]/(c_{v,tr}\rho) \tag{13}$$

where $c_{v,tr} = \sum \sigma_i c_{v,tr,i}$. Combining equations (12) and (13), we obtain the following expressions for the partial derivatives of pressure:

$$\begin{aligned} \frac{\partial P}{\partial(\rho E)} = \left(\frac{R\sigma}{c_{v,tr}}\right) = \beta,\quad \frac{\partial P}{\partial(\rho e_v)} = -\beta,\quad \frac{\partial P}{\partial(\rho u)} = -\beta u,\quad \frac{\partial P}{\partial(\rho v)} = -\beta v \\ \frac{\partial P}{\partial \rho_i} = \beta\left[(u^2+v^2)/2 - e_{tr,i}\right] + RT/M_i \\ = -\beta e_{tr,i} + RT/M_i + \beta(u^2+v^2)/2 \\ = \alpha_i + \beta(u^2+v^2)/2 \end{aligned} \tag{14}$$

where $\alpha_i = RT/M_i - \beta e_{tr,i}$. These partial derivatives of P will be used in the solution algorithm.

Speed of sound is another variable required in the present analysis. An expression for the speed of sound can be obtained starting from the first principles. In problems with nonequilibrium flows, the appropriate speed of sound is the frozen speed of sound (see Ref. 7) defined by

$$c^2 = \left.\frac{\partial P}{\partial \rho}\right|_{S,\bar{q}} \tag{15}$$

where S is the entropy of the gas mixture and $\bar{q}$ are the nonequilibrium variables, namely the mole numbers of the species and the vibrational energy. For a mixture of gases, the entropy is given by

$$S = \sum s_i \sigma_i - R\sigma\left[ln\,(p/p_0) - \sum ln\,(\sigma/\sigma_i)\right] \tag{16}$$

and the entropy, s_i, of each of the species is given by

$$s_i = \frac{dh_i}{T} \tag{17}$$

If the vibrational energy is held constant, then we can write

$$ds_i = c_{p,tr,i}\frac{dT}{T} \tag{18}$$

Differentiating Eqn. (16) with constant σ_i, and substituting for ds_i from Eqn. (18), we obtain

$$dS = \sum c_{p,tr,i}\sigma_i\frac{dT}{T} - R\sigma\frac{dP}{P} \tag{19}$$

Also, upon differentiating the equation of state with constant σ_i yields

$$\frac{dP}{P} = \frac{d\rho}{\rho} + \frac{dT}{T} \tag{20}$$

Now setting $dS = 0$, eliminating dT between Eqns. (19) and (20), and using the relation $c_{p,tr,i} = R - c_{v,tr,i}$, we find

$$\frac{dP}{P} = \frac{d\rho}{\rho} + \frac{R\sigma}{\sum c_{p,tr,i}\sigma_i}\frac{dP}{P} = \frac{d\rho}{\rho} + \frac{\beta}{\beta+1}\frac{dP}{P} \tag{21}$$

Hence

$$c^2 = \left(\frac{\partial P}{\partial \rho}\right)\Big|_{S,\bar{q}} = (\beta+1)\,P/\rho \tag{22}$$

Next, consider the expression

$$\begin{aligned}\sum \alpha_i x_i + \beta h - \beta e_v &= \sum (RT/M_i - \beta e_{tr,i})\,x_i + \beta h - \beta e_v \\ &= RT\sigma - \beta e_{tr} + \beta h - \beta e_v \\ &= P/\rho - \beta e_{tr} + \beta\,(e_{tr} + e_v + P/\rho) - \beta e_v \\ &= (\beta+1)\,P/\rho\end{aligned} \tag{23}$$

Therefore, the speed of sound in nonequilibrium flow can be expressed as

$$c = \sqrt{\sum \alpha_i x_i + \beta (h - e_v)} \tag{24}$$

TRANSPORT PROPERTIES

A procedure for computation of the transport properties of a multicomponent gas mixture has been described by Gnoffo, et al. (Ref. 1), which in turn is based on Lee's formulation (Ref. 2). These computations require evaluation of two collision integrals. These collision integrals depend only on the translational temperature, T, for atomic and molecular particles, (electrons are absent in the present analysis), and are evaluated as curve fits using the tabulated data also from Ref. 1. We follow the procedure of Gnoffo, et al. (Ref. 1) for the computation of viscosity and thermal conductivity of the gas mixture, and binary diffusion coefficients of the 5 species. This procedure is summarized here.

Values of the two collision integrals $\Omega_{i,j}^{(k,k)}$, $k = 1, 2$, at temperatures of 2,000 K and 4,000 K are available in tabular form in Ref. 1. Assuming a linear variation for $\log\left[\pi\Omega_{i,j}^{(k,k)}\right](T)$ with $\log(T)$, the following expression is obtained:

$$\log\left[\pi\Omega_{i,j}^{(k,k)}\right](T) = \log\left[\pi\Omega_{i,j}^{(k,k)}\right](2000) + slope \times ln(T/2000) \tag{25}$$

where

$$slope = \left[\log\left[\pi\Omega_{i,j}^{(k,k)}\right](4000) - \log\left[\pi\Omega_{i,j}^{(k,k)}\right](2000)\right]/ln(2) \tag{26}$$

The modified collision integrals used in the evaluation of the transport properties are defined as follows:

$$\Delta_{i,j}^{(1)}(T) = \frac{8}{3}\left[\frac{2m_{i,j}}{\pi RT}\right]^{1/2}\pi\Omega_{i,j}^{(1,1)} \tag{27}$$

$$\Delta_{i,j}^{(2)}(T) = \frac{16}{5}\left[\frac{2m_{i,j}}{\pi RT}\right]^{1/2}\pi\Omega_{i,j}^{(2,2)} \tag{28}$$

where $m_{i,j}$ is the reduced molecular weights of species i and j, and is defined by

$$m_{i,j} = M_i M_j/(M_i + M_j) \tag{29}$$

Viscosity:

Viscosity of the gas mixture is given by

$$\mu = \sum_{i=1}^{5} \frac{m_i \sigma_i}{\sum_{j=1}^{5} \sigma_j \Delta_{i,j}^{(2)}(T)} \tag{30}$$

Thermal Conductivity:

The translational energy mode is assumed fully excited; hence the translational energy thermal conductivity is given by

$$\eta_t = \frac{15}{4} k \sum_{i=1}^{5} \frac{\sigma_i}{\sum_{j=1}^{5} a_{i,j} \sigma_j \Delta_{i,j}^{(2)}(T)} \tag{31}$$

where the constant $a_{i,j}$ is defined as

$$a_{i,j} = 1 + \frac{(1 - M_i/M_j)\,[0.45 - 2.54\,(M_i/M_j)]}{(1 + M_i/M_j)^2} \tag{32}$$

The rotational energy mode is also assumed to be fully excited; hence the rotational energy thermal conductivity is given by

$$\eta_r = k \sum_{i=mol} \frac{\sigma_i}{\sum_{j=1}^{5} \sigma_j \Delta_{i,j}^{(1)}(T)} \tag{33}$$

The frozen thermal conductivity is the sum of η_t, and η_r. The vibrational energy mode, however, is assumed to be partially excited; hence the vibrational thermal conductivity is computed following the procedure given in Gupta, et al. (Ref. 3) as follows:

$$\eta_v = k \sum_{i=mol} \frac{(c_{v,v,i}/R)\,\sigma_i}{\sum_{j=1}^{5} \sigma_j \Delta_{i,j}^{(1)}(T)} \tag{34}$$

However, when the vibrational energy mode becomes fully excited, $c_{v,v,i} = R$, and $\eta_v = \eta_r$, which is the relation given in Ref. 1.

Mass Diffusion Coefficient:

The effective mass diffusion coefficient, D_i, of species i in the gas mixture is given by

$$D_i = \frac{\sigma^2 M_i (1 - \sigma_i M_i)}{\sum_{j=i}^{5} \sigma_j / D_{i,j}} \tag{35}$$

where $D_{i,j}$ is the binary diffusion coefficient for a pair of particles of species i and j, and is related to the modified collision integral as follows:

$$D_{i,j} = \frac{kT}{p\Delta_{i,j}^{(1)}(T)} \tag{36}$$

VIBRATIONAL AND RELAXATION PROCESSES

Millikan and White (Ref. 8) give the following semi-empirical correlation for the vibrational relaxation time

$$P\tau_i^M = \left\{ \sum_{j=1}^{5} n_j exp\left[A_j \left(T^{-1/3} - 0.015 m_{i,j}^{1/4} \right) - 18.42 \right] \right\} / \sum_{j=1}^{5} n_j \tag{37}$$

where $m_{i,j}$ is the reduced molecular weight defined in Eqn. (29). The values of the constants A_j are 129 for O_2, 220 for N_2, and 168 for NO. The relaxation times computed by the above relation are valid over a temperature range of 300 to 8,000 K. At temperatures beyond 8,000 K, the above relation yields relaxation times much smaller than observed in experiments. For temperatures above 8,000 K, Park (Ref. 9) suggests the following relation for the vibrational relaxation time:

$$\tau_i^P = 1/(\Omega_i n_i \bar{c}_i) \tag{38}$$

where Ω_i is the effective collision cross section for vibrational relaxation (following Park, Ref. 9, this is set equal to 10^{-16} cm^2), n_i is the number density of species i, and $\bar{c}_i$ is the average velocity of molecules i, given by

$$\bar{c}_i = [8kT/(\pi m_i)]^{1/2} \tag{39}$$

Blending of the two relations Eqns. (37) and (38) gives the following expression for the vibrational relaxation time:

$$\tau_i = \tau_i^M + \tau_i^P \tag{40}$$

Park points out that this expression for vibrational relaxation time is applicable over a much wider temperature range.

CHEMICAL KINETIC MODEL

The nonequilibrium chemistry effects involving the five chemical species are modeled by 17 kinetic steps listed in Table 1. The rate of production of species i is given by the following expression:

$$\dot{w}_i = \sum_{j=1}^{17} (\nu'_{i,j} - \nu_{i,j}) \, (R_{f,j} - R_{b,j}) \tag{41}$$

where $\nu_{i,j}$ and $\nu'_{i,j}$ are the stoichiometric coefficients for the i-th species in the j-th reaction for reactants and products, respectively, and $R_{f,j}$ and $R_{b,j}$ are the forward and backward reaction rates, respectively, for the j-th reaction. The reaction rates are given by the following:

$$\begin{aligned} R_{f,j} &= k_{f,j} \prod_{i=1}^{5} (\rho_i / M_i)^{\nu'_{i,j}} \\ R_{b,j} &= k_{b,j} \prod_{i=1}^{5} (\rho_i / M_i)^{\nu_{i,j}} \end{aligned} \tag{42}$$

where $k_{f,j}$ and $k_{b,j}$ are the forward and backward reaction rate constants. These rate constants are, in general, functions of the translational and vibrational temperatures, see Park (Ref. 10), for example. In addition, there is a chemical-vibrational coupling. However, in the present analysis, the reaction rate constants are assumed to be functions of translational temperature only, and are expressed as follows:

$$k_{f,j} = A_j T^{n_j} exp\,(-d_j / T) \tag{43}$$

The constants A_j, n_j, and d_j for the 17 kinetic steps are obtained from Gnoffo and McCandless (Ref. 11), and are also listed in Table 1. The backward reaction rate constants are obtained from the relation

$$K_{e,j} = k_{f,j} / k_{b,j} \tag{44}$$

$K_{e,j}$ is the equilibrium constant for the kinetic step j. These equilibrium constants for the 17 kinetic steps are determined using the following relation:

$$K_{e,j} = exp\,(-\Delta G_j / RT) \tag{45}$$

where ΔG_j is the net change in the Gibbs energy in reaction j, and is expressed as

$$\Delta G_j = \sum_i (\nu'_{i,j} - \nu_{i,j}) \, G_i \tag{46}$$

where G_i is the standard state Gibbs energy of formation of the i-th species. This may be computed (by noting that $G_i = h_i - Ts_i$) by the following expression:

$$G_i = RT\left[a_{i,1}(1-\log(T)) + a_{i,6}/T - a_{i,7} - \sum_{j=2}^{5} a_{i,j}T^{j-1}/j(j-1)\right] \tag{47}$$

Note that contributions from only the translational temperature to h_i and s_i are considered. The constants $a_{i,j}, i = 1, \ldots, 5, j = 1, \ldots, 7$ are the constants that appear in the curve fits for the heat capacity of the five species, and are taken from Prabhu and Erickson (Ref. 6).

METHOD OF SOLUTION

The method of solution employed is this paper is based on the method described by Thareja, et al. (Ref. 4) which is an unstructured mesh implementation of a cell centered upwind scheme using Roe's flux difference splitting technique for the inviscid terms of the governing equations for perfect gas. The procedure has also been extended to equilibrium flows by Prabhu, et al. (Ref. 12). We briefly describe the procedure as it is applied to the equations governing non-equilibrium flows.

The governing equations are written in the following compact form:

$$\frac{\partial U}{\partial t} + \frac{\partial F}{\partial x} + \frac{\partial G}{\partial y} = W \tag{48}$$

Note that the transport terms are not included here; they will be treated separately, and

$$\begin{aligned} U^T &= \{\rho_i, \rho u, \rho v, \rho E, \rho e_v\} \\ F^T &= \{\rho_i u, P + \rho u^2, \rho uv, \rho uH, \rho ue_v\} \\ G^T &= \{\rho_i v, \rho uv, P + \rho v^2, \rho vH, \rho ve_v\} \\ W^T &= \{\dot{w}_i, 0, 0, 0, \sum_{i=mol} \rho_i (e^*_{v,i} - e_{v,i})/\tau_i + \sum_{i=mol} \dot{w}_i \hat{D}_i\} \end{aligned} \tag{49}$$

Also note that the source like terms on the right hand side of the vibrational energy conservation equation have been included in the vector W. These terms are: (1) energy relaxation between vibrational and translational modes, and (2) vibrational energy lost/gained due to molecular depletion/production within a cell.

The computational domain is subdivided into triangular and/or quadrilateral elements. The unknowns, U, are assumed to be constant over each element, and the governing equations are

integrated over each element.

$$\int\left(\frac{\partial U}{\partial t}+\frac{\partial F}{\partial x}+\frac{\partial G}{\partial y}=W\right)d\Omega_e \tag{50}$$

The time-derivative is linearized, and the above equation is rewritten as follows:

$$\frac{(U^{m+1}-U^m)}{\Delta t}\Omega_e+\int\left(\frac{\partial F}{\partial x}+\frac{\partial G}{\partial y}\right)^{m+1}d\Omega_e = W^{m+1}\Omega_e \tag{51}$$

Indices m and m+1 refer to two consecutive time levels. Upon replacing the area integral of the derivatives with the appropriate contour integrals, we obtain

$$\frac{\Delta U}{\Delta t}\Omega_e+\oint F_n^{m+1}d\Gamma = W^{m+1}\Omega_e \tag{52}$$

The quantity F_n is the component of the inviscid flux normal to a side. The unknowns are discontinuous across each side. The flux across such a face is given by

$$F_n^{m+1} = \left[F_{n,e}^{m+1}+F_{n,r}^{m+1}-|A|\left(U_r^{m+1}-U_e^{m+1}\right)\right]/2 \tag{53}$$

where the subscript e refers to the element under consideration and the subscript r refers to the element sharing the common side. The quantities $F_{n,e}$ and $F_{n,r}$ are the fluxes normal to the side under consideration. The matrix $|A|$ is defined as

$$|A| = R|\Lambda|R^{-1} \tag{54}$$

where R and R^{-1} are the right and the left eigenvector matrices of the flux Jacobian matrix, A. The matrix $|\Lambda|$ is the diagonal matrix of the eigenvalues of A, with all negative values replaced by corresponding positive values. This introduces upwind bias. The matrix A must be evaluated at each element interface, and should exhibit Roe's property U (see Roe, Ref. 13). Upon substituting Eqn. (53) in Eqn. (52), replacing the contour integral by a summation over the sides of the element, and rearranging, we find

$$\frac{\Delta U}{\Delta t}\Omega_e+\sum_{sides}\left[F_{ne}^{m+1}+F_{nr}^{m+1}-|A|\left(U_r^{m+1}-U_e^{m+1}\right)\right]\delta_s/2 = W^{m+1}\Omega_e \tag{55}$$

where δ_s is the length of the side. Linearization of the above equation gives the following scheme.

$$\left[I+\frac{\Delta t}{2\Omega_e}\sum_s|A^*|\delta_s\right]\Delta U = -\frac{\Delta t}{2\Omega_e}\sum_s\left[F_{ne}^m+F_{nr}^*-|A^*|\left(U^*_r-U_e^m\right)\right]\delta_s-W^m\Omega_e \tag{56}$$

The values with an asterisk as the index are those computed using most recent values in the ele-

ment and its neighbors. This makes the scheme point implicit. Evaluation of the matrix A at the cell interface forms a major part of the computations, and is discussed in the following paragraphs.

THE JACOBIAN AND RELATED MATRICES

Gnoffo, et al. (Ref. 1) have derived the inviscid flux Jacobian and eigenvector matrices for nonequilibrium flows in 3-D. They include ionic species and electrons in their chemistry model. We adopt their formulation simplifying it for 2-D flows with only five chemical species. The component of the inviscid flux normal to a side of an element is given by

$$F_n = Fn_x + Gn_y \tag{57}$$

where n_x and n_y are the x- and y-components of the unit outward normal to the side. The inviscid flux Jacobian defined by $A = \partial F_n / \partial U$ can be derived, and is given by

$$[A] = \begin{bmatrix} (\delta_{i,j} - x_i)\,U & x_i n_x & x_i n_y & 0 & 0 \\ (\alpha_j + \beta q)\,n_x - Uu & (1-\beta)\,un_x + U & (1-\beta)\,vn_x - V & \beta n_x & -\beta n_x \\ (\alpha_j + \beta q)\,n_y - Uv & (1-\beta)\,un_y + V & (1-\beta)\,vn_y + U & \beta n_y & -\beta n_y \\ (\alpha_j + \beta q - H)\,U & Hn_x - \beta Uu & Hn_y - \beta Uv & (1+\beta)\,U & -\beta U \\ -Ue_v & e_v n_x & e_v n_y & 0 & U \end{bmatrix} \tag{58}$$

The Kronecker delta function, $\delta_{i,j}$ has the usual meaning, i.e., $\delta_{i,j} = 1$ if $i = j$, $\delta_{i,j} = 0$ otherwise. In Eqn. (58), the index i=1,...,5 refers to the rows and the chemical species, and the index j=1,...,5 refers to the columns and the chemical species. Also $U = un_x + vn_y$, $V = vn_x - un_y$, and $q = (u^2 + v^2)/2$. The matrix A is a square matrix of order 9. The eigenvalues of A are

$$\Lambda = [U \ (repeated\ 6\ times), (U+c), (U-c), U] \tag{59}$$

where c is the speed of sound given by $c = \sqrt{\sum \alpha_i x_i + \beta\,(H - q - e_v)}$. Note that only three of these values, namely U, $U+c$, and $U-c$, are distinct. The right eigenvector matrix of A corresponding to the eigenvalues given by Eqn. (59) is

$$\frac{[R]}{c^2} = \begin{bmatrix} \delta_{i,j} & 0 & x_i/2 & x_i/2 & 0 \\ u & -n_y & (u + cn_x)/2 & (u - cn_x)/2 & 0 \\ v & -n_x & (v + cn_y)/2 & (v + cn_y)/2 & 0 \\ (\beta q - \alpha_j) & V & (H + cU)/2 & (H - cU)/2 & 1 \\ 0 & 0 & e_v/2 & e_v/2 & 1 \end{bmatrix} \tag{60}$$

The inverse of the matrix R given by R^{-1} is also required, and is given by

$$[R^{-1}] = \begin{bmatrix} c^2\delta_{ij} - x_i(\alpha_j + \beta q) & -\beta u x_i & -\beta v x_i & -\beta x_i & \beta x_i \\ -V & -n_y & n_x & 0 & 0 \\ \alpha_j + \beta q + Uc & cn_x - \beta u & cn_y - \beta v & \beta & -\beta \\ \alpha_j + \beta q - Uc & -cn_x - \beta u & -cn_y - \beta v & \beta & -\beta \\ -e_v(\alpha_j + \beta q) & -\beta u e_v & -\beta v e_v & -\beta e_v & c^2 + \beta e_v \end{bmatrix} \tag{61}$$

It can be verified that $R\Lambda R^{-1} = A$, and $RR^{-1} = I$, where I is the identity matrix. Note that the matrices A, R, and R^{-1} must be evaluated at the so called Roe-averaged state. The variables at the Roe-averaged state are designated by an overbar, and are determined as follows:

One of the properties that the matrix $\bar{A} = A(\bar{U})$ must satisfy is

$$\Delta(F_n) = \bar{A}\Delta(U) \tag{62}$$

where $\Delta(\ ) = (\ )_R - (\ )_L$. Equation (62) has nine components corresponding to the nine components of $\Delta(F_n)$. The first five components of these are satisfied if we define

$$\begin{aligned} \bar{x}_i &= a(x_i)_L + b(x_i)_R \qquad i = 1, \ldots, 5 \\ \bar{u} &= au_L + bu_R \qquad \bar{v} = av_L + bv_R \end{aligned} \tag{63}$$

where

$$a = \sqrt{\rho_L}/(\sqrt{\rho_R} + \sqrt{\rho_L}), \qquad b = \sqrt{\rho_R}/(\sqrt{\rho_R} + \sqrt{\rho_L}) \tag{64}$$

Note that $a + b = 1$, and that

$$\sum \bar{x}_i = a\sum (x_i)_L + b\sum (x_i)_R = a + b = 1 \tag{65}$$

This is a necessary condition if the x_i's are to retain the property of mass fraction. The sixth and the seventh components of Eqn. (62) are satisfied provided the following condition is satisfied.

$$\Delta(P) = \sum_{i=1}^{5} \bar{\alpha}_i \Delta(\rho_i) + \bar{\beta}\Delta(\rho e_{tr}) \tag{66}$$

Finally, the eighth and the ninth components are satisfied if we define

$$\begin{aligned} \bar{H} &= aH_L + bH_R \\ \bar{e}_v &= a(e_v)_L + b(e_v)_R \end{aligned} \tag{67}$$

It now remains to determine $\bar{\alpha}_i$ and $\bar{\beta}$. The method of determining these is not obvious, since the only condition they have to satisfy is Eqn. (66). In all the available literature, there is no rigorous method for the determination of these quantities. Methods based on either some approximations (see Liu and Vinocur, Ref. 14) or on computational experience (see Gnoffo, Ref. 15)

have been suggested. We describe here a simple, yet accurate method to determine these quantities. The basis for the present method is the requirement that $\bar{\alpha}_i$ and $\bar{\beta}$ together with the other Roe-average variable form a consistent set of thermodynamic variable.

Since β depends only on the mass fractions, x_i, we require that $\bar{\beta}$ be related to $\bar{x}_i$ by the same functional relation. Hence, $\bar{\beta}$ can be determined from the known values of $\bar{x}_i$, i.e.,

$$\bar{\beta} = \left[\sum_{i=1}^{5} \bar{x}_i / M_i\right] / \left[\sum_{i=1}^{5} f_i \bar{x}_i / M_i\right] \tag{68}$$

where $f_i = 2.5$ for molecular species, and 1.5 for atomic species. Similarly, we require that the relation between $\bar{\alpha}_i$ and other variables be the same as the relation between α_i and other variables. Since $\alpha_i = RT/M_i - \beta e_{tr,i}$, we write

$$\bar{\alpha}_i = R\bar{T}/M_i - \bar{\beta} e_{tr,i} \tag{69}$$

Note that $\bar{e}_{tr,i}$ the is sum of translational, rotational, and formation energies, and is related to the correspond temperature $\bar{T}$ by the following relation:

$$\begin{aligned} \bar{e}_{tr,i} &= (2.5R\bar{T} + \Delta h_{f,i})/M_i \qquad \textit{for molecules} \\ &= (1.5R\bar{T} + \Delta h_{f,i})/M_i \qquad \textit{for atoms} \end{aligned} \tag{70}$$

Therefore, $\bar{\alpha}_i, i = 1, \ldots, 5$ are linear functions of $\bar{T}$. Upon using these relations in Eqn. (66), and solving the resulting equation for $\bar{T}$, we obtain the following:

$$\bar{T} = \frac{\Delta(P) - \bar{\beta}\Delta(\rho e_{tr}) + \bar{\beta}\sum_{i=1}^{5} \Delta h_{f,i} \Delta(\rho_i)/M_i}{\sum_{i=1}^{5} R(1 - f_i\bar{\beta})\Delta(\rho_i)/M_i} \tag{71}$$

where, as before, $f_i = 2.5$ for molecular species, and 1.5 for atomic species. All the terms on the right hand side of the above equation are known; hence, $\bar{T}$ can be readily computed. Once $\bar{T}$ is determined, $\bar{e}_{tr,i}$ can be determined using Eqn. (70). Next, Eqn. (69) provides the values of $\bar{\alpha}_i$. Thus, $\bar{\alpha}_i, i = 1, \ldots, 5$ and $\bar{\beta}$ are computed such that the necessary condition Eqn. (66) is satisfied exactly.

Before proceeding further, it is necessary to show that the temperature, $\bar{T}$, computed by the above equation is always positive. We demonstrate this in the following manner:

We note that $\Delta(P) = (P)_R - (P)_L$, $\Delta(\rho_i) = (\rho_i)_R - (\rho_i)_L$, and $\Delta(\rho e_{tr}) = (\rho e_{tr})_R - (\rho e_{tr})_L$.

Substituting these relations, and the expression for $\bar{\beta}$ from Eqn. (68) in Eqn. (71), and upon considerable simplification, we find

$$\bar{T} = aT_L + bT_R \tag{72}$$

This is a remarkably simple result, and confirms that $\bar{T}$ is positive, and bounded by T_L and T_R.

The speed of sound can now be determined using the following relation:

$$\bar{c} = \sqrt{\sum \bar{\alpha}_i \bar{x}_i + \bar{\beta}(\bar{H} - \bar{q} - \bar{e}_V)} \tag{73}$$

where $\bar{q} = \left(\bar{u}^2 + \bar{v}^2\right)/2$. Since all the quantities on the r. h. s. of Eqn. (73) are known, $\bar{c}$ can be computed.

The value of $\bar{c}$ computed by Eqn. (73) must be positive. To verify this, we start with the definition of $\bar{H}$

$$\bar{H} = aH_L + bH_R = ah_L + bh_R + \bar{q} + \Delta \tag{74}$$

where, it can be shown that

$$\Delta = ab\left[(u_L - u_R)^2 + (v_L - v_R)^2\right]/2 \geq 0 \tag{75}$$

Next, we substitute $h = e_{tr} + e_V + P/\rho$ in Eqn. (74), and obtain the following:

$$\begin{aligned} \bar{H} &= a\left[(e_{tr})_L + (e_V)_L + (P/\rho)_L\right] + b\left[(e_{tr})_R + (e_V)_R + (P/\rho)_R\right] + \bar{q} + \Delta \\ &= \bar{e}_{tr} + \bar{e}_V + \overline{(P/\rho)} + \bar{q} + \Delta \end{aligned} \tag{76}$$

where $\bar{e}_{tr} = a(e_{tr})_L + b(e_{tr})_R$ and $\overline{(P/\rho)} = a(P/\rho)_L + b(P/\rho)_R$. Next, we consider the definition of $\bar{c}$ and write

$$\bar{c}^2 = \sum \bar{\alpha}_i \bar{x}_i + \bar{\beta}(\bar{H} - \bar{q} - \bar{e}_V) \tag{77}$$

Upon substituting for $\bar{\alpha}_i$ and $\bar{H}$ from Eqns. (69) and (76), respectively, and simplifying, we find

$$\bar{c}^2 = \bar{\beta}(\bar{\varepsilon} + \overline{(P/\rho)} + \Delta) \tag{78}$$

where $\bar{\varepsilon} = a\varepsilon_L + b\varepsilon_R$, and $\varepsilon = RT\sum f_i x_i / W_i$. All the quantities on the right hand side of Eqn. (78) are positive, hence $\bar{c}^2$ is positive.

Thus, all the unknowns in the Roe-averaged state required to compute the matrices $\bar{A}$, $\bar{R}$, and $\bar{R}^{-1}$ are determined. No approximations were made determining $\bar{\alpha}$, $\bar{\beta}$, and other variables at the Roe-averaged state. These variables namely, $\bar{x}_i, i = 1, \ldots, 5, \bar{u}, \bar{v}, \bar{H}, \bar{e}_v, \bar{\alpha}_i, i = 1, \ldots, 5$, $\bar{\beta}$ and $\bar{c}$ form a consistent set of thermodynamic variables, and satisfy the necessary condition Eqn. (66)

exactly.

TRANSPORT TERMS

All the transport terms, namely the viscous, heat conduction, and mass diffusion terms in the governing equations are treated implicitly in essentially the same way as in Thareja, et al. (Ref. 4). Similarly, the species production terms are also treated implicitly. These details are not included here. The reader is directed to Ref. 4 for information pertaining to the treatment of transport terms.

RESULTS AND DISCUSSIONS

Mach 15 flow past a 2.54 mm radius cylindrical body with and without shock interference were considered. The following examples were solved:

(1) Undisturbed flow

(2) Type IV shock interference flow

In both cases, the freestream conditions were assumed to be as follows:

Velocity	4,678 m/s
Density	0.00922 kg/m^3
Temperature	241 K
Mach number	15
Reynolds number	7,500

Since the Reynolds number is low, the flow is assumed to laminar everywhere. For the shock interference case, the impinging oblique shock angle is 8.88 deg. The location of the impinging shock is assumed to be as shown in Fig. 2. Other flow properties in that stream are as follows:

Velocity	4,628 m/s
Density	0.02863 kg/m^3
Temperature	473 K
Mach number	10.6
Flow inclination	6 deg. (up)

Wall temperature for both the cases is assumed to be 811 K. These conditions as well as the loca-

tions of the impinging shock are very close to the conditions used by Carlson and Wilmoth (Refs. 16 and 17), who studied these problems using Direct Simulation Monte Carlo (DSMC) method. This facilitated a direct comparison of present results with those from Carlson and Wilmoth. Both fully catalytic and noncatalytic walls were considered in the present work, and the wall catalytic effects are evaluated. A fully catalytic wall was assumed to have the property that all the atoms that came into contact with it recombined into molecules. The fully catalytic wall was assumed to have no effect on nitric oxide.

Mesh Requirements:

The adaptive remeshing strategy of LARCNESS yields satisfactory meshes for flow problems dominated by shock waves. It provided adequate meshes for the case of undisturbed flow (with no impinging shock) past the body. Since the undisturbed flow is symmetric about the x-axis, flow over 1/2 of the body (1/4 cylinder) was computed. Computations were made on a sequence of meshes, each finer than the previous until the peak heat flux on the body remained practically unchanged on two successive meshes. The final mesh used in this case (not shown) has a total of 17,884 elements consisting of triangles and quadrilaterals.

In a Type IV shock-shock interference flow the primary flow features are two triple points, two shear layers that originate at these triple points, and a supersonic jet that undergoes repeated expansion and compression. The procedure of adaptive remeshing employed in LARCNESS, captures the strong shocks, but does not capture the weaker shocks and the shear layer. With the adaptive remeshing it was possible to capture the bow shock and the transmitted shock in front of the body. The regions covered by shear layers and the terminating normal shock, however, needed local mesh enrichments.

As in the previous example, computations were made on a sequence of meshes, each finer than the previous until the peak heat flux on the body remained practically unchanged on two successive meshes. The contour plots of flow variable from an initial mesh provided information for adaptive remeshing as well as for refinement. The shear layers were identified from the (u/u_∞) contour plots, and these regions were uniformly refined. Uniform refinement subdivides each triangular element into four smaller ones. The final mesh used in the present computations has the following properties:

Total number of nodes	85,293
Total number of elements	155,960
Number of triangular elements	142,069
Number of quadrilateral elements	13,891
Total number of sides in the triangles mesh	213,441
Number of sides with length < 0.00254 mm	11,876
Number of sides with length < 0.00508 mm	82,453

In this mesh, a large fraction of the total number of elements is in the region of the two shear layers and the supersonic jet. The length of the upper shear layer was measured from the *u*-velocity contour plots; its length was 1.0 mm (approx.). It may be recalled that the radius of the cylindrical body is 2.54 mm. Following the procedure of Glass (Ref. 18), the shear layer thickness was estimated to be 0.076 mm, using the known flow conditions downstream of the bow shock and assuming laminar flow. (It may be recalled that the freestream Reynolds number based on the body radius is 1500; hence it was assumed that the flow is laminar everywhere.) Similarly, the thickness of the lower shear layer was estimated to be 0.0254 mm. (Note that these shear layer originate at their respective triple points with zero thickness.) Triangular elements with sides of the order of 0.0025 mm were considered adequate to resolve flow in shear layers of this thickness.

The mesh has 29 layers of quadrilateral elements next to the body. This part of the mesh helps in accurate determination of the velocity and temperature gradients in the boundary layer. The thickness of the first layer is 2.54×10^{-6} mm, and the total thickness of the quadrilateral elements layer is 0.245 mm. There are 480 points along the circumference of the body, with an average spacing of 0.376 deg. between points, and a minimum spacing of about 0.056 deg. near the jet impingement region. This spacing captured the steep temperature gradients in the stagnation region.

Example 1- Undisturbed Flow:

The results for Mach 15 flow past a 2.54 mm radius cylindrical body are shown in Figs. 3-11, for the fully catalytic as well as the noncatalytic walls. The contours of (u/u_∞), Mach number, and translational and vibrational temperatures for the fully catalytic wall case are shown in Figs. 3(a) - 3(d). These plots display smooth contours of flow variables. The maximum translational

temperature in the flowfield is 9,937 K, and the maximum vibrational temperature is 5,251 K.

Contours of O2, O, N2, and N mole fraction for the fully catalytic wall case are shown in Figs. 4(a) - 4(d). These plots indicate that oxygen is almost completely dissociated behind the normal part of the bow shock. However, only a small part of nitrogen is dissociated. Figures 5(a) & 5(b) and 6(a) & 6(b) show similar plots for the noncatalytic wall. No noticeable differences may be seen between these plots and the corresponding plots for the catalytic wall. The maximum translational temperature is 9,918 K and maximum vibrational temperature is 5,256 K (which are close to the corresponding values for the fully catalytic wall). The wall catalytic effects are not felt away from the wall.

The variation of mole fractions along the center line are shown in Figs. 7(a) and 7(b) for the fully catalytic and the noncatalytic walls, respectively. As noted earlier from the contour plots, oxygen is almost completely dissociated between the bow shock and the body. However, all of the oxygen atoms recombine as the flow reaches the fully catalytic wall. In the case of the noncatalytic wall, although the wall is relatively cold (T_w= 811 K), only some of the oxygen atoms recombine into oxygen molecules. This is the result of chemical nonequilibrium. Between the bow shock and the body, there is some nitrogen dissociation; but all of the nitrogen atoms recombine for fully catalytic as well as the noncatalytic walls. For the noncatalytic walls, the recombination of nitrogen atoms is due to the low wall temperature. Mole fraction of nitric oxide is not noticeably affected by the wall catalytic effects. The effect of the wall catalyticity is confined to a region very close to the wall. The shock stand-off distance in both cases is about 0.26 r.

Variations of (u/u_∞), (T/T_∞), and (T_v/T_∞) along the centerline (line of symmetry) are shown in Figs. 8 and 9, respectively. The u-velocity drops sharply as the flow passes through the shock, after which it decrease steadily and reaches zero at the stagnation point. The translational temperature rises steeply through the shock, and reaches its peak value immediately behind the shock. In contrast, the vibrational temperature rises slowly through the shock. This trend is to be expected. Behind the shock, as the flow goes towards the stagnation point, the translational temperature drops from its peak value and the vibrational temperature rises. This is the consequence of thermal nonequilibrium. As the flow approaches the stagnation point, both the temperatures drop sharply, and reach the specified value of 811 K at the wall. The wall catalytic effects have very little effect on velocity and temperature variations along the center line. Very close to the wall, however, there are significant differences in the temperature distributions between the catalytic and the noncatalytic walls which lead to differences in the surface heat fluxes.

Distribution of pressure amplification (P/P_{t2}) on the body is shown in Figs. 10. It may be observed that the pressure distribution on the body is unaffected by the wall catalytic effects. At the stagnation point the value of (P/P_{t2}) is 1.028 implying that the pressure at the stagnation point for this nonequilibrium flow is about 2.8% higher than the corresponding value for perfect gas. The losses in the total pressure through the normal shock in front of the body, seem to be smaller for nonequilibrium flow compared to the perfect gas case. The value of P_{t2} is easily computed, and is equal to 186 kPa. Hence the stagnation point pressure is 191 kPa.

The heat flux distribution on the body for the fully catalytic and noncatalytic walls is shown in Fig. 11. The surface heat flux for the fully catalytic wall is significantly higher than for the noncatalytic wall. The peak values are 20.4 MW/m^2 for the catalytic wall and 15.9 MW/m^2 for the noncatalytic wall. Unlike the pressure distribution, the heat flux distribution curves are not smooth, particularly near the stagnation point. This behavior could not be explained. The very large aspect ratio of the elements near the stagnation point is suspected to be one of the causes of this.

Carlson and Wilmoth (Refs. 16 and 17) solved this problem using a DSMC approach and assuming a noncatalytic wall. The stagnation point pressure and heat flux obtained by them are 200 kPa and 15 MW/m^2, respectively, which compare very well with the corresponding values of 191 kPa and 15.9 MW/m^2 obtained by the present computations.

Example 2- Type IV Shock Interference Flow:

The results for Type IV shock interference flow at Mach 15 past a cylindrical body of 2.54 mm radius are shown in Figs. 12 - 20. The mole fraction contours of O2 and O are shown in Fig. 12, and the mole fraction contours of N2 and N are shown in Fig. 13. These plots are for the fully catalytic wall; corresponding plots for the noncatalytic wall are not presented as they were not noticeably different from the plots for the fully catalytic wall except very close to the wall. The wall catalytic effect does introduce differences in the gas composition close to the wall. This will be discussed later in this section. As in the case of undisturbed flow, most of the oxygen is dissociated behind the normal shock, whereas only a small amount of nitrogen is dissociated.

Contour plots of (u/u_∞) and Mach number are shown in Fig. 14, and the contour plots of translational and vibrational temperature are shown on Fig. 15. These contour plots are for the catalytic wall; there are no noticeable differences between these contours plots and the corresponding plots for the noncatalytic wall. The two triple points, the two shear layers, and the jet

terminating normal shock may be seen in these figures. The maximum translational temperature is 10,082 K, and is reached as the flow passes through the normal part of the bow shock above the impinging oblique shock. The maximum vibrational temperature is 5,594 K. The maximum translational temperature is close to the corresponding value for the undisturbed flow (9,937 K). This is to be expected, since the maximum temperature occurs as the flow passes through the normal shock.

The pressure contours in the flow field are shown on Figs. 16a and 16b. The two triple points, the transmitted shock, and a compression and an expansion of the flow (before it reaches the terminating normal shock) may be seen in Fig. 16a. An enlarged view of the pressure contours near the stagnation point is shown in Fig. 16b. The normal shock that terminates the supersonic jet may be seen clearly in this figure. This normal shock is essentially parallel to the wall, and hence is expected to lead to the most severe heating on the body. The peak pressure on the body is at θ = -16.7 deg. The pressure on the body over a one-degree interval (θ = -16 deg. to -17 deg.) is essentially constant. It may be noted that this region lies right behind the normal shock. The pressure contours for the noncatalytic wall are not shown; there is no noticeable differences between the pressure contours for the catalytic and noncatalytic wall cases.

The pressure distributions on the body for the catalytic and the noncatalytic walls are shown in Figs. 17a and 17b. The wall catalytic effects do not seem to affect noticeably, either the peak pressure or the pressure distribution on the body. Although the pressure distribution appears to have a sharp peak, Fig. 17a, the peak value is essentially constant over a one-degree range - between θ = -16 deg. and -17 deg. (See Fig. 17b). As noted earlier, this corresponds to the region covered by the terminating normal shock of the supersonic jet. The value of the pressure peak is about 13.1 times the pressure at the stagnation point for undisturbed flow of a perfect gas, and occurs at θ = -16.7 deg. on the body (also see the pressure contours, Fig. 16b). With P_{t2} equal to 186 kPa, the maximum pressure is 2,440 kPa.

The heat flux distributions for the catalytic and the noncatalytic walls are shown in Figs. 18a and 18b. Similar to the pressure distribution, the heat flux distribution also exhibits a sharp peak (See Fig. 18a). A closer examination of this peak, however, reveals some details (Fig. 18b). Unlike the pressure distribution, the heat flux distribution for the fully catalytic wall is significantly higher than for the noncatalytic wall. Also, the distributions have two peaks - one at θ = -16 deg. and the other at θ = -17 deg. Recall that this region (between θ = -16 deg. and -17 deg.) over which the pressure is practically constant, corresponds to the region covered by the normal

shock terminating the supersonic jet. The probable cause of this particular shape of the heat flux distribution with two peaks is discussed in a following paragraph. The peak value is 544 MW/m^2 for the catalytic wall and 431 MW/m^2 for the noncatalytic wall. At the fully catalytic wall, all the atoms recombine into molecules. Atomic recombination reactions are exothermic; the heat released during recombination causes higher temperature gradients at the wall resulting in higher heat fluxes.

The skin friction distribution on the body is shown if Fig. 19. It may be noted from this figure that the skin friction is zero at θ = -16.7 deg. indicating that the stagnation point is at this location on the body. The distribution also displays two peaks in skin friction values - one at θ = -15.5 deg. and the other at θ = -17.7 deg. These locations are close to the peak heat flux locations. The mass flow in the supersonic jet, after passing through the terminating normal shock, is divided into two parts - one going up and the other going down along the body. These accelerating flows exiting the stagnation region (between the jet terminating shock and the body) seem to cause locally high skin friction. The high skin friction values perhaps lead to the two peaks in the heat flux distribution.

Carlson and Wilmoth predict a peak pressure of 2,900 kPa (approx.) and a peak heat flux of 530 MW/m^2 for the shock interference case with the noncatalytic wall (see Fig. 9, Ref. 17). The corresponding values from present computations are 2,440 kPa and 431 MW/m^2, and are lower than the DSMC computations. The location of the peak pressure on the body also differs - the present computations show the peak at -16.7 deg. whereas the DSMC results show the peak at around -19 deg. The temperature and Mach number contours in the two flowfields, however, appear similar. (Compare Figs. 8a and 8b from Ref. 17 with the present Figs. 15c and 15b). One of the significant differences in the two studies is that flow properties in the stream below the incident shock are somewhat different in the two cases. In the present computations those conditions were obtained by assuming an inviscid flow past a 6 deg. wedge, whereas Carlson and Wilmoth computed those conditions using a nonequilibrium DSMC code with no boundary layer on the wedge. This would result in differences in the flow properties in that stream which in turn could lead to differences in surface pressure and heat fluxes. The present results, however, show considerable details of the flowfield, particularly near the jet terminating shock and the stagnation region. This has been possible due to the very fine grids employed in the present computations. Such details are not seen in the DSMC results.

Pressure and heat flux distributions were computed for Type IV shock interference in a perfect gas (See Prabhu, Ref. 19). Those results were obtained using a highly refined mesh of about 235,000 elements, and yielded a peak pressure 2,301 kPa and a peak heat flux of 529 MW/ m^2. Although the impinging shock location in that case was the same as in the present case, the normal shock that terminates the jet was not parallel to the body. This is primarily because the stand-off distance of the bow shocks in front of the body is much larger for perfect gas than for corresponding nonequilibrium flows. Larger stand-off distance in the perfect gas case caused wider supersonic jet. The pressure as well as the heat flux distributions for the perfect gas case are skewed, suggesting that the impinging shock location did not correspond to the worst stagnation point heating condition.

Variations of pressure, density, translational and vibrational temperatures, and mole fraction of the constituent gases as the flow passes through the jet terminating normal shock and reaches the stagnation point (along the Cut A-A shown in Fig. 16) are shown in Figs. 20a - 20d. The pressure rises quite sharply as the flow passes through the normal shock after which as the flow reaches the surface, the pressure gradually rises to its peak value (see Fig. 20a). The density also rises through the normal shock, but rises very sharply through the boundary layer. This is because the pressure is essentially constant through the boundary layer whereas the temperature drops very rapidly. The translational and vibrational temperature distributions (Fig. 20b) are similar to what was noticed for the undisturbed flow (compare this figure with Fig. 9). Similarly, the mole fraction distributions for the fully catalytic wall as well as that for the noncatalytic wall, shown in Figs. 20c and 20d, are similar to what was observed for undisturbed flow (see Figs. 8a & 8b). These similarities are to be expected since in the both the cases the flow is passing through a normal shock and reaching a stagnation point at the wall.

CONCLUDING REMARKS

The governing equations for chemical and thermal nonequilibrium flow, and some details of the solution algorithm which employs a point-implicit, cell-centered, upwind scheme are presented. The solution employs Roe's flux difference splitting method for the inviscid fluxes. The method for implementing the scheme on an unstructured meshes is included. Air is treated as a reacting gas mixture of 5 chemical species namely O2, N2, O, NO, and N. Ions and electrons are neglected. Two temperatures namely translational-rotational and vibrational are assumed to describe the thermodynamic energy. Since the rotational characteristic temperatures for the con-

stituent species are small, the translational and rotational energy modes are assumed to be in equilibrium, whereas the vibrational energy mode is assumed to be in nonequilibrium. A harmonic oscillator model is assumed to characterize the vibrational energy of molecular species.

The computational domain was discretized using unstructured triangular elements and several layers of structured quadrilateral elements on the body. Structured layers of quadrilateral elements placed next to the body surface enable capturing large gradients in the flow quantities in the boundary layer. The part of mesh with triangular elements is obtained adaptively, and further refined for the shock interference case to enable capturing complex flow features. Several layers of quadrilateral elements were placed next to the wall to enable capturing the boundary layer features well. The thickness of the first quadrilateral element layer was 2.54×10^{-6} mm, with a minimum spacing of 0.056 deg. along the circumference of the body. The final mesh employed had 155,960 elements - the smallest element had a side length of 0.00254 mm. This may be compared with the body radius of 2.54 mm. It has been possible to obtain detailed flow features and heat flux and pressure distributions primarily because of this adapted and highly refined meshes.

Details of the complex flow features associated with Type IV shock interference could be seen in the contours plots of the flow variables. The triple points, the shear layers, the supersonic jet, and the terminating normal shock may be seen clearly in those plots. For the conditions in the example, the results indicate that oxygen is almost fully dissociates behind the bow shock in front of the body. For the catalytic wall case the oxygen atoms recombine at the wall. A part of nitrogen also undergoes dissociation; however, the nitrogen atoms recombine at the wall conditions. The pressure distribution plot exhibits a small region of high pressure on the body (where the supersonic jet impinges). The peak pressure is approximately 13.1 times the pitot pressure in perfect gas. The heat flux distribution exhibits two peaks of almost equal magnitude within a small region (also corresponding to the jet impingement region). The peak heat flux is 544 MW/m^2 for the catalytic wall and 431 MW/m^2 for the noncatalytic wall. The effect of a catalytic wall was primarily to increase the heat flux on the body. The corresponding numbers for undisturbed flow (with no shock interference) are 20.4 MW/m^2 for the catalytic wall and 15.9 MW/m^2 for the noncatalytic wall.

The adaptive remeshing procedure works satisfactorily for strong shocks, but is unable to capture weak shocks and shear layers. It was therefore necessary to refine the regions of shear layers and weak shocks manually to enable resolving these flow features. Refining the mesh in these regions was necessary for adequately resolving these flow features and obtaining accurate

results. The present solution algorithm is only first order accurate, and a higher order solution algorithm would perhaps require a less refined mesh.

Present results for the undisturbed flow case compared well with DSMC computations. However, the results for the shock interference case (location and magnitudes of the peak pressure and the peak heat flux) differed from the DSMC computations. It is possible that factors including the differences in the post incident shock flow properties and differences in computational grids could have contributed to the differences in the results.

ACKNOWLEDGEMENTS

The author wishes to express his appreciation to Dr. Peter A. Gnoffo of NASA Langley Research Center for many useful discussions.

REFERENCES

1. Gnoffo, P. A., Gupta, R. N., and Shinn, J. L.: 'Conservation Equations and Physical Models for Hypersonic Flows in Thermal and Chemical Nonequilibrium,' NASA Technical Paper 2867, Langley Research Center, Hampton, VA, February 1989.

2. Lee, J. H.: 'Basic Governing Equations for the Flight Regimes of Aeroassisted Orbital Transfer Vehicles,' *Thermal Design of Aeroassisted Transfer Vehicles*, Progress in Astronautics and Aeronautics, Vol. 96, AIAA, 1985, pp. 3-53.

3. Gupta, R. N., Yos, J. M., Thompson, R. A., and Lee, K. P.: 'A Review of Reaction Rates and Thermodynamic and Transport Properties for an 11-Species Air Model for Chemical and Thermal Nonequilibrium Calculations to 30 000 K,' NASA Reference Publication 1232, Langley Research Center, Hampton, VA, August 1990.

4. Thareja, R. R., Stewart, J. R., Hassan, O., Morgan, K., and Peraire, J.: 'A Point Implicit Unstructured Grid Solver for the Euler and Navier-Stokes Equations,' *International Journal for Numerical Methods in Fluids*, Vol. 9, 1989, pp. 405-425.

5. Edney, B.: 'Anomalous Heat Transfer and Pressure Distributions on Blunt Bodies at Hypersonic Speeds in the Presence of an Impinging Shock,' FFA Report 115, The Aeronautical Research Institute, Sweden, February 1968.

6. Prabhu, R. K. and Erickson, W. D.: 'A Rapid Method for the Computation of Equilibrium Chemical Composition of Air to 15 000 K,' NASA Technical Paper 2792, Langley Research Center, Hampton, VA, March 1988.

7. Vincenti, W. G. and Kruger, Jr., C. H.: '*Introduction to Physical Gas Dynamics*,' Published by John Wiley and Sons, New York, 1965.

8. Millikan, R. C. and White, R. R.: 'Systematics of Vibrational Relaxation,' *Journal of Chemical Physics*, Vol. 39, No. 12, December 1963, pp. 3209-3213.

9. Park, C.: 'Problems of Rate Chemistry in the Flight Regimes of Aeroassisted Orbital Transfer Vehicles,' *Thermal Design of Aeroassisted Transfer Vehicles*, Progress in Astronautics and Aeronautics, Vol. 96, AIAA, 1985, pp. 511-537.

10. Park, C.: 'Assessment of Two-Temperature Kinetic Model for Ionizing Air,' AIAA Paper No. 87-1574, June 1987.

11. Gnoffo, P. A. and McCandless, R. S.: 'Three-Dimensional AOTV Flowfields in Chemical Nonequilibrium,' AIAA Paper No. 86-0230, Presented at the AIAA 24th Aerospace Sciences Meeting, January 1986, Reno, NV.

12. Prabhu, R. K., Stewart, J. R., and Thareja, R. R.: 'A Navier-Stokes Solver for High Speed Equilibrium Flows and Application to Blunt Bodies,' AIAA Paper No. 89-0668, Presented at the 27th Aerospace Sciences Meeting, January 9-12, 1989, Reno NV.

13. Roe, P. L.: 'Approximated Riemann Solvers, Parameter Vector, and Difference Schemes,' *Journal of Computational Physics*, Vol. 43, 1981, pp. 357-372.

14. Liu, Y. and Vinocur, M.: 'Upwind Algorithms for General Thermo-Chemical Nonequilibrium Flows,' AIAA Paper No. 89-0201, Presented at the 27th Aerospace Sciences Meeting, January 9-12, 1989, Reno NV.

15. Gnoffo, P. A.: 'Upwind-Biased, Point-Implicit Relaxation Strategies for Viscous Hypersonic Flows,' AIAA Paper No. 89-1972-CP, 1989.

16. Carlson, A. B. and Wilmoth, R. G.: 'Shock Interference Prediction Using Direct Simulation Monte Carlo,' *Journal of Spacecraft and Rockets*, Vol. 29, No. 6, November-December 1992; Also AIAA Paper No. 92-0492.

17. Carlson, A. B. and Wilmoth, R. G.: 'Monte Carlo Simulation of a Near-Continuum Shock-Shock Interaction Problem,' *Journal of Spacecraft and Rockets*, Vol. 31, No. 1, January-February 1994.

18. Glass, C. E.: 'Computer Program to Solve Two-Dimensional Shock-Wave Interference Problems with an Equilibrium Chemically Reacting Air Model,' NASA Technical Memorandum

4187, Langley Research Center, Hampton, VA, August 1990.

19. Prabhu, R. K.: 'Chemical and Thermal Nonequilibrium CFD Solutions using Unstructured Grids for Type IV Shock Interference Heating on Cowl Lip,' NASP Contractor Report 1162, NASA Langley Research Center, Hampton, VA, September 1994.

Table 1: Reaction Rate Constants

j	*Reaction*	A_j	N_j	D_j
1	O2+O2 <=> O+O+O2	23.243e+13	-1.0	59,500
2	O2+N2 <=> O+O+N2	7.200e+12	-1.0	59,500
3	O2+O <=> O+O+O	9.000e+13	-1.0	59,500
4	O2+NO <=> O+O+NO	3.600e+12	-1.0	59,500
5	O2+N <=> O+O+N	3.600e+12	-1.0	59,500
6	N2+O2 <=> N+N+O2	1.900e+11	-0.5	113,500
7	N2+N2 <=> N+N+N2	24.700e+11	-0.5	113,500
8	N2+O <=> N+N+O	1.900e+11	-0.5	113,500
9	N2+NO <=> N+N+NO	1.900e+11	-0.5	113,500
10	N2+N <=> N+N+N	4.085e+16	-0.5	113,500
11	NO+O2 <=> N+O+O2	3.900e+14	-1.5	75,500
12	NO+N2 <=> N+O+N2	23.900e+14	-1.5	75,500
13	NO+O <=> N+O+O	27.800e+15	-1.5	75,500
14	NO+NO <=> N+O+NO	27.800e+15	-1.5	75,500
15	NO+N <=> N+O+N	27.800e+15	-1.5	75,500
16	NO+O <=> N+O2	23.200e+03	1.0	19,700
17	N2+O <=> NO+O	0.000e+07	0.0	38,000

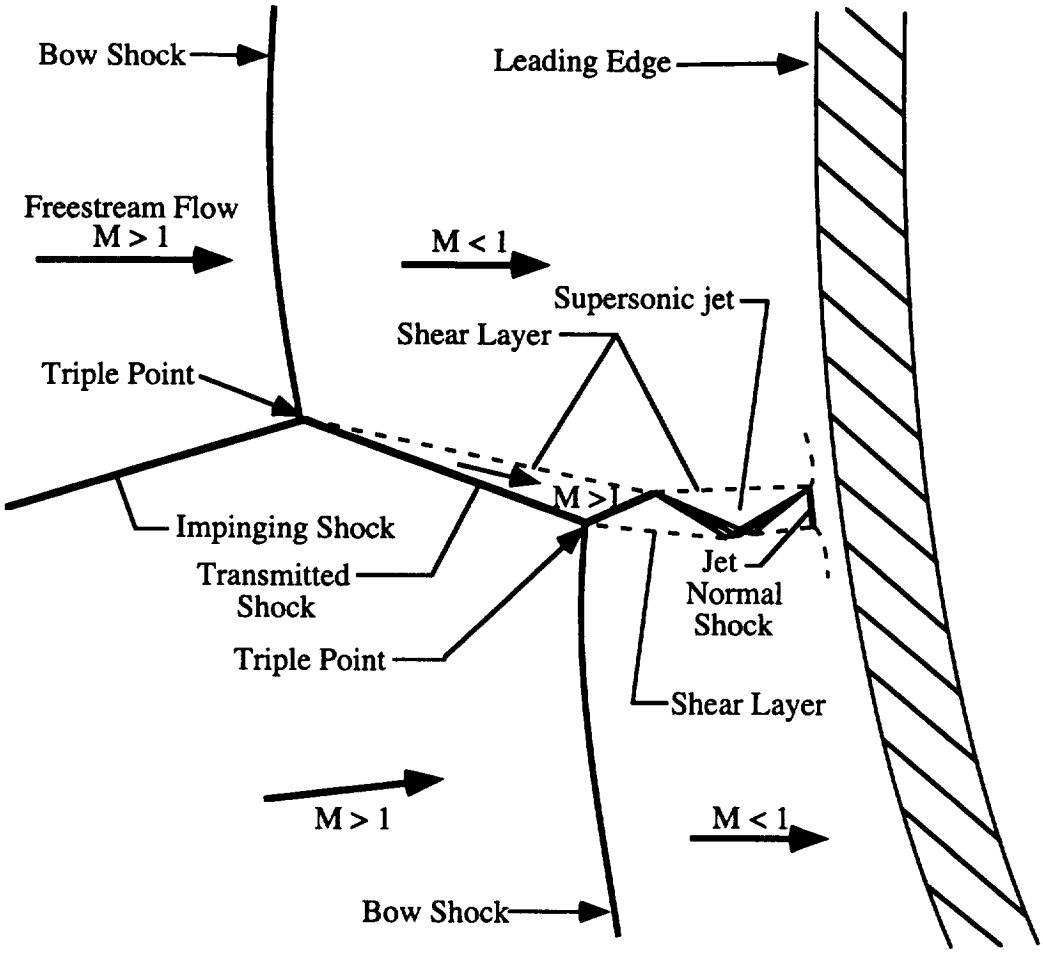

Figure 1. Type IV supersonic jet interference pattern

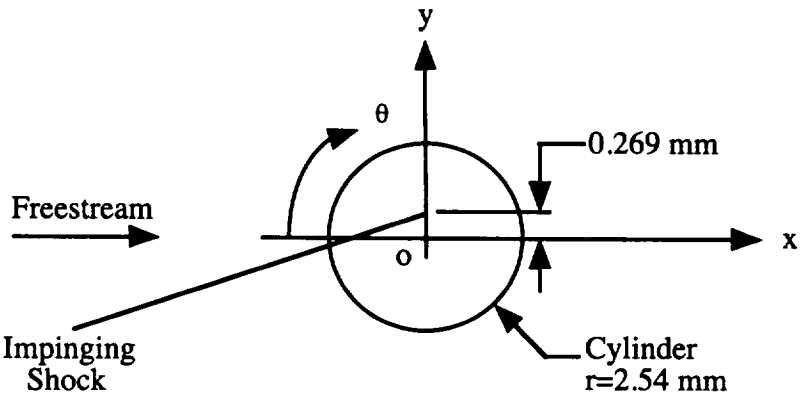

Figure 2. Schematic of the problem

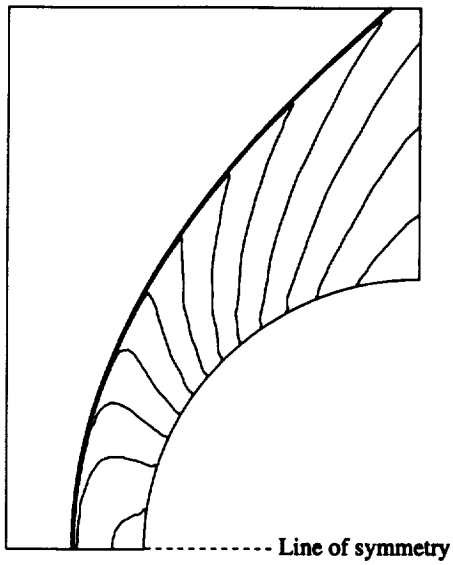

(a) Contours of (u/u_∞)

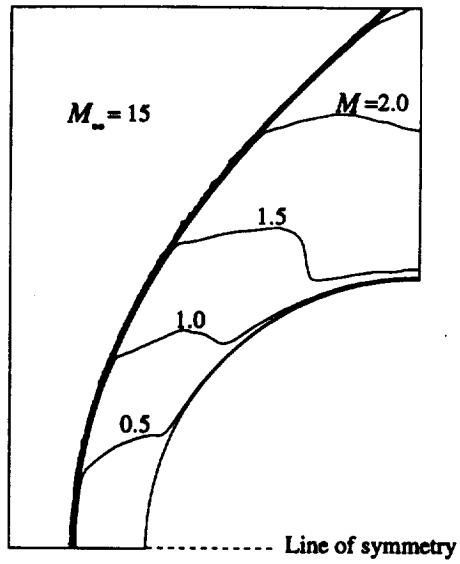

(b) Mach number contours

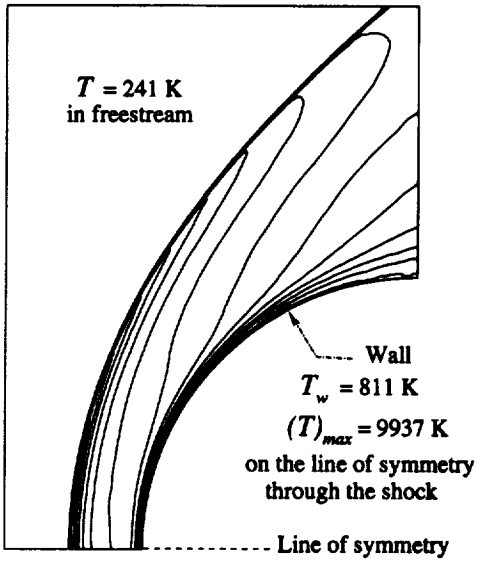

(c) Translational temperature contours

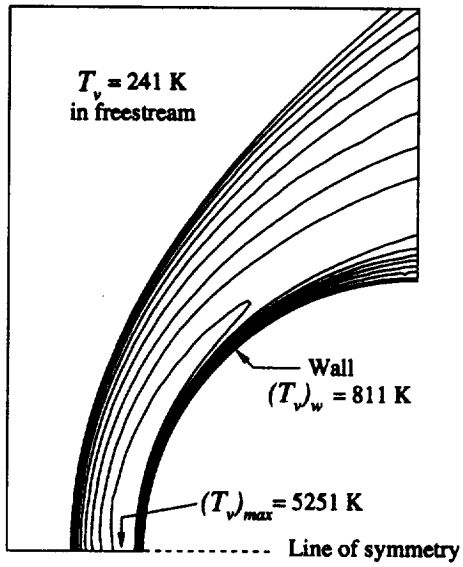

(d) Vibrational temperature contours

Figure 3. Contours of u-velocity, Mach number, and translational and vibrational temperatures for Mach 15 undisturbed flow (fully catalytic wall)

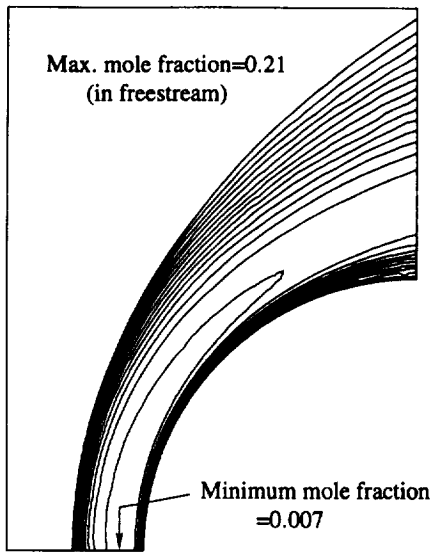

(a) O2 mole fraction contours

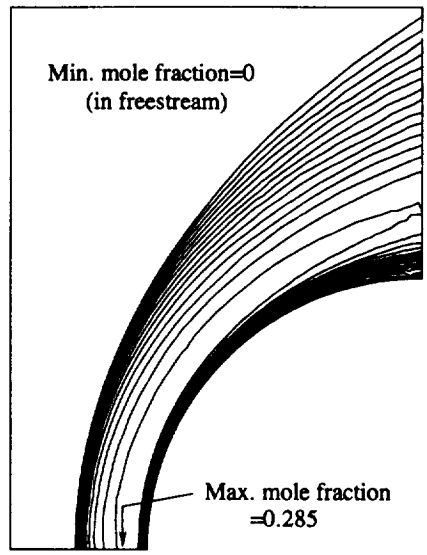

(b) O mole fraction contours

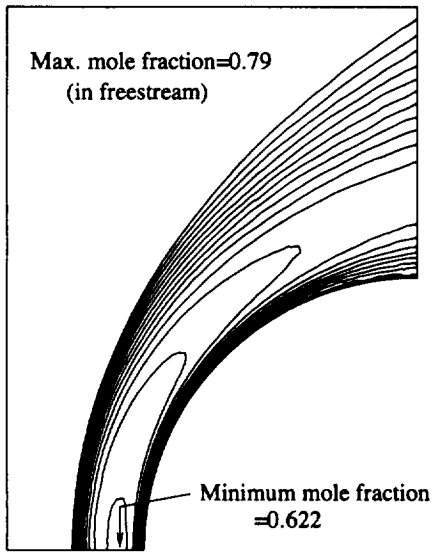

(c) N2 mole fraction contours

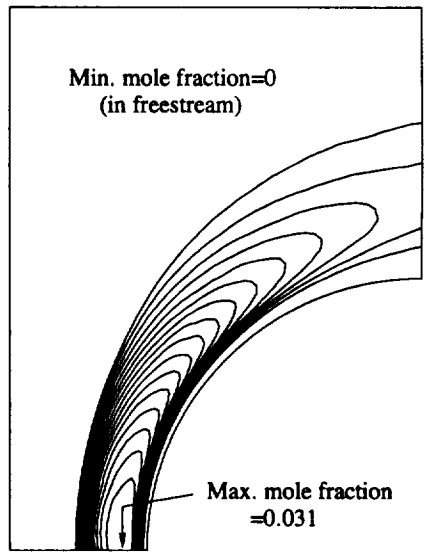

(d) N mole fraction contours

Figure 4. O2, O, N2, and N Mole fraction contours for Mach 15 undisturbed flow (fully catalytic wall)

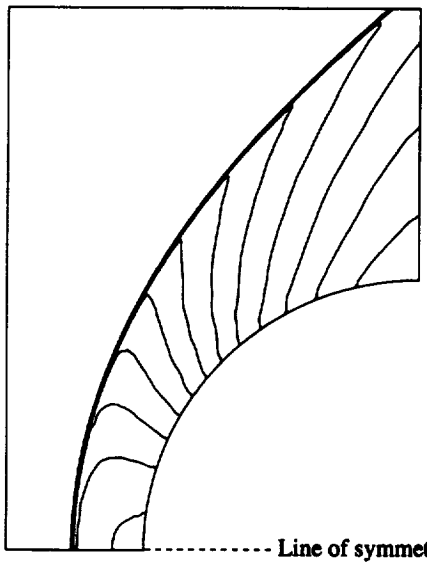

(a) Contours of (u/u_∞)

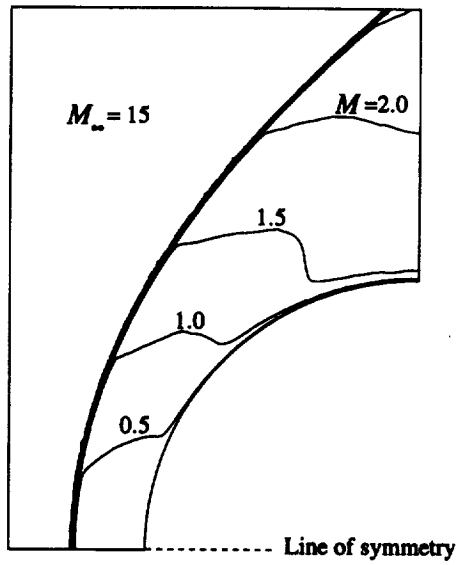

(b) Mach number contours

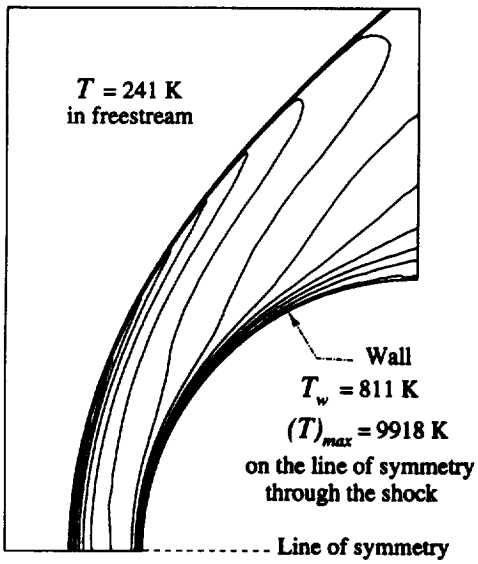

(c) Translational temperature contours

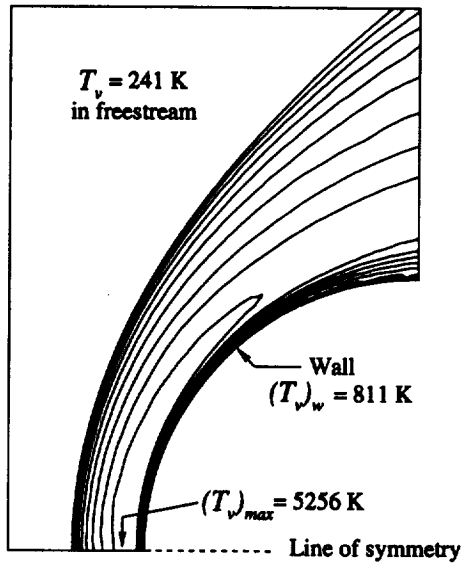

(d) Vibrational temperature contours

Figure 5. Contours of u-velocity, Mach number, and translational and vibrational temperatures for Mach 15 undisturbed flow (noncatalytic wall)

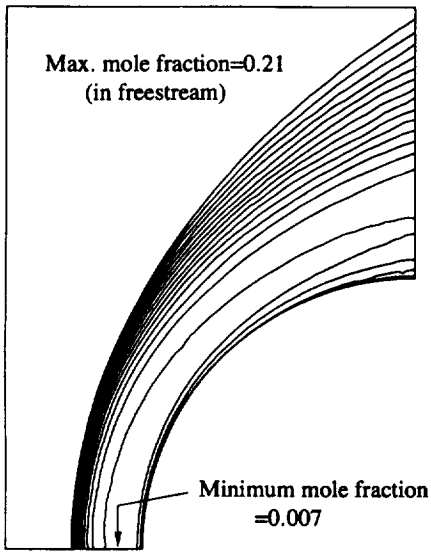

(a) O2 mole fraction contours

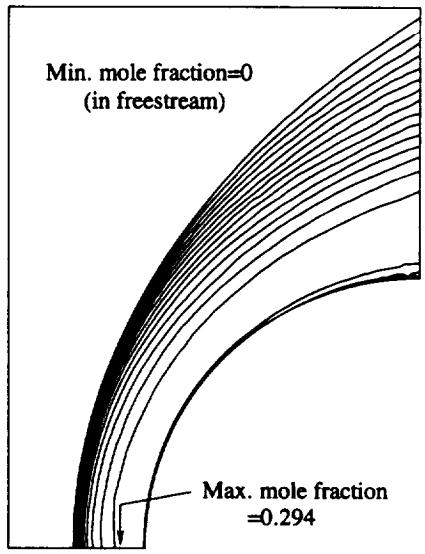

(b) O mole fraction contours

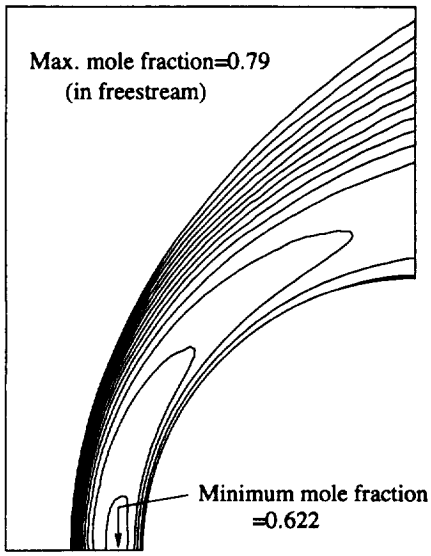

(c) N2 mole fraction contours

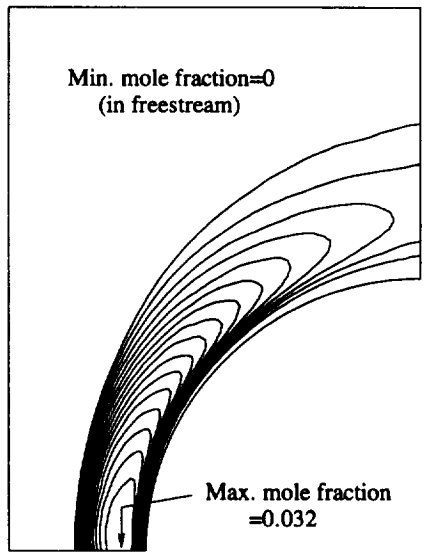

(d) N mole fraction contours

Figure 6. O2, O, N2, and N Mole fraction contours for Mach 15 undisturbed flow (noncatalytic wall)

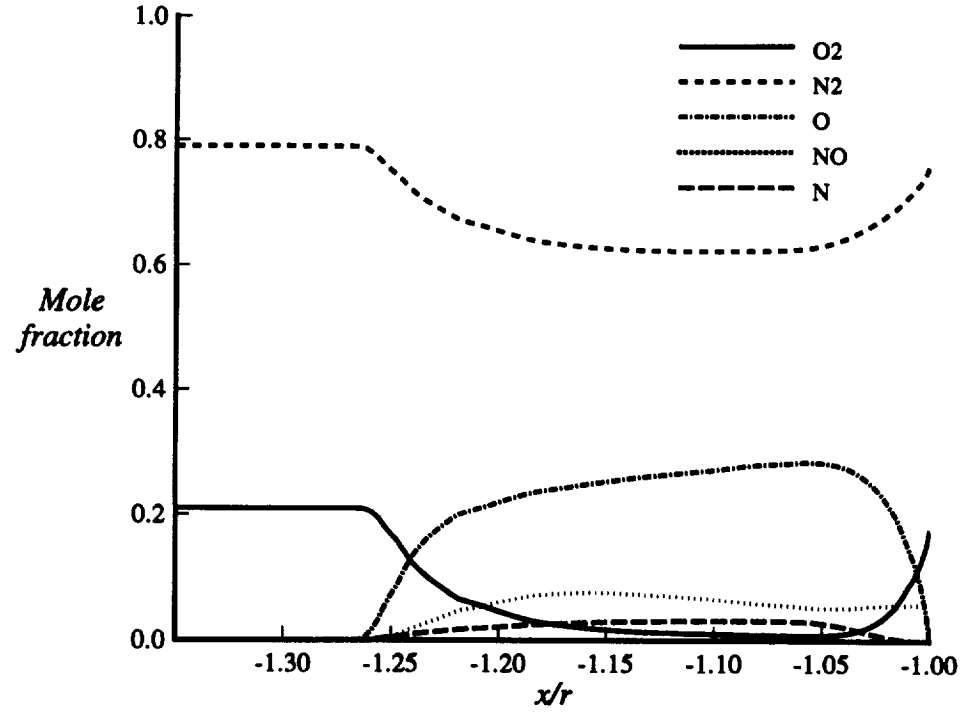

Figure 7a. Mole fraction distributions on the centerline for Mach 15 undisturbed flow (fully catalytic wall)

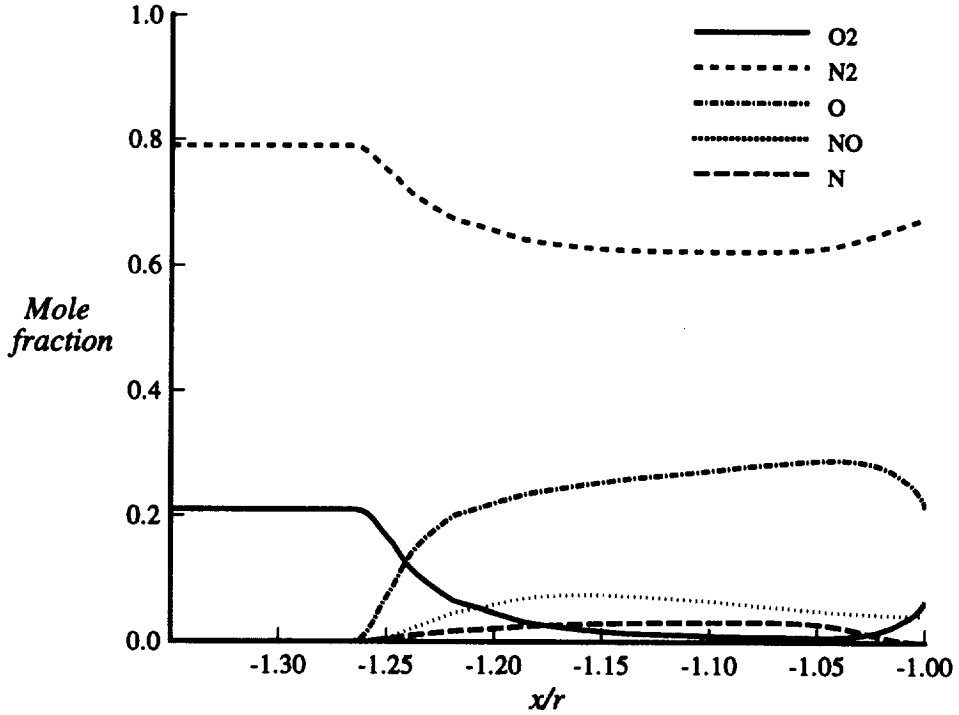

Figure 7b. Mole fraction distributions on the centerline for Mach 15 undisturbed flow (noncatalytic wall)

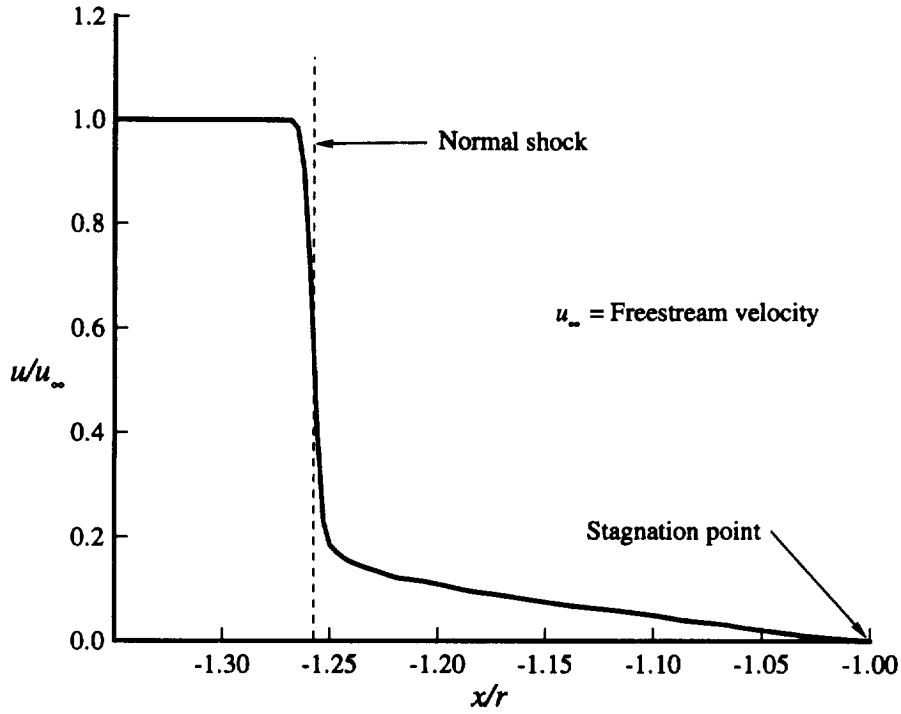

Figure 8. u-velocity distribution on the centerline for Mach 15 undisturbed flow (fully catalytic and noncatalytic walls)

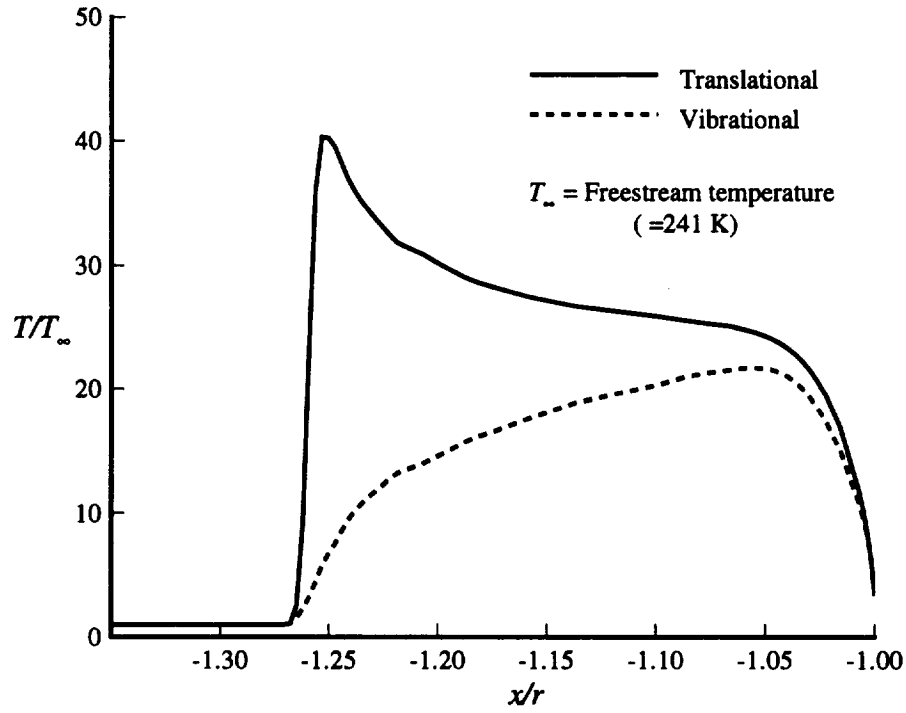

Figure 9. Temperature distributions on the centerline for Mach 15 undisturbed flow (catalyitc and noncatalytic walls)

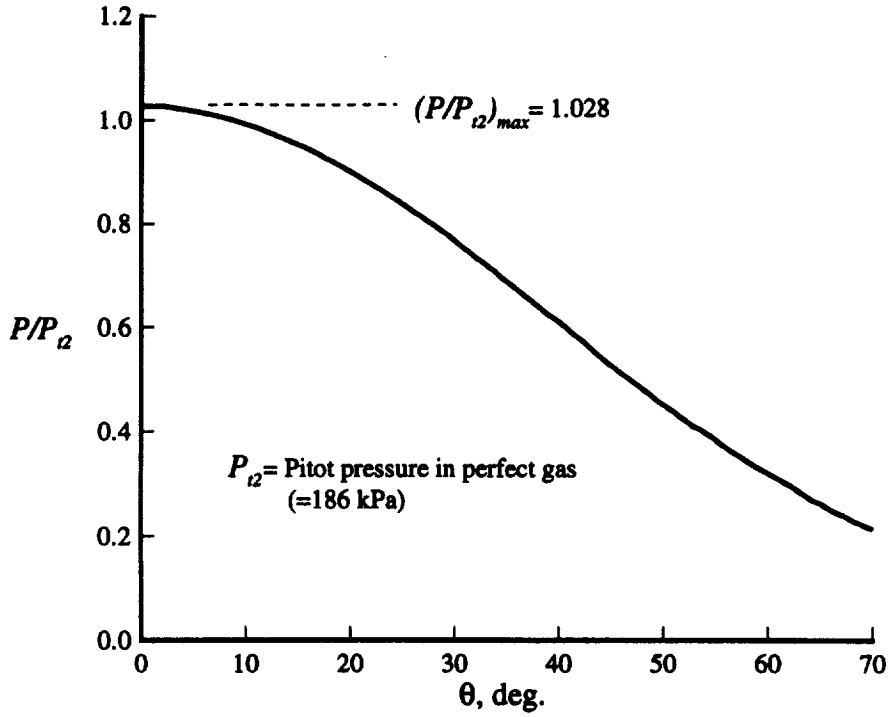

Figure 10. Pressure distribution on a 0.1 inch radius cylindrical body in Mach 15 flow (catalytic and noncatalytic walls)

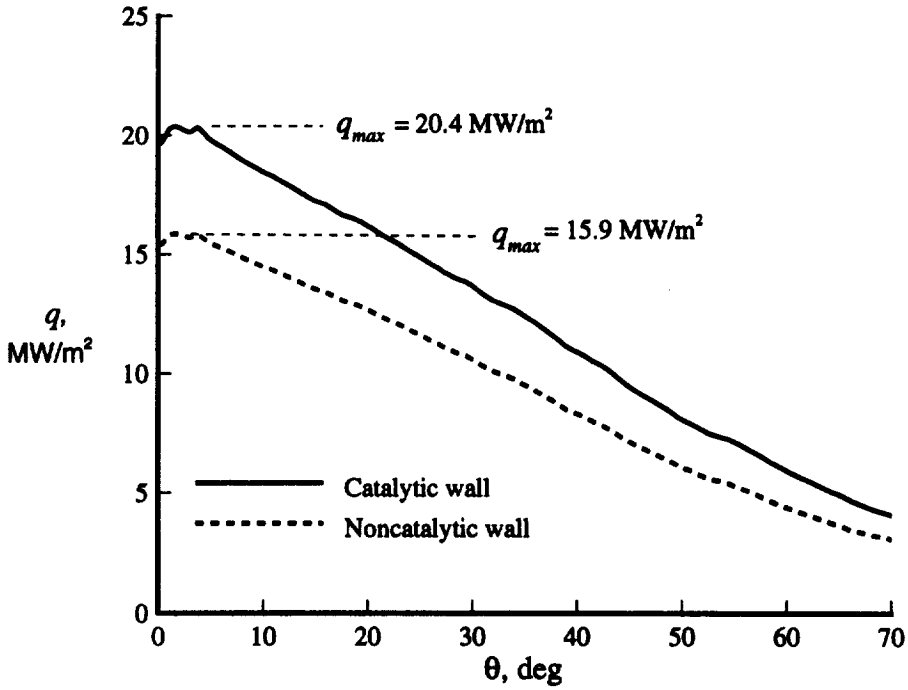

Figure 11. Heat flux distribution on a 0.1 inch radius cylindrical body in Mach 15 flow

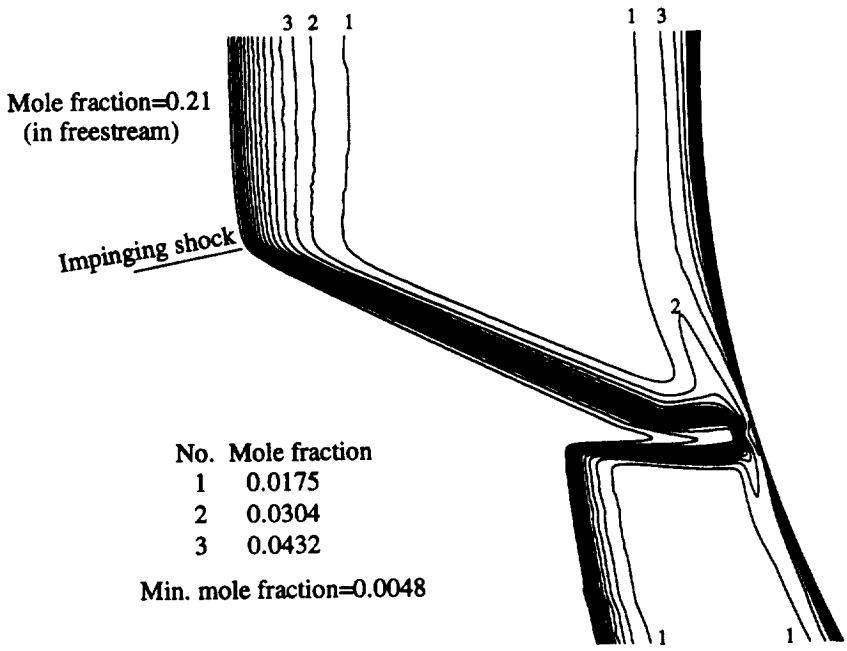

(a) O2 mole fraction

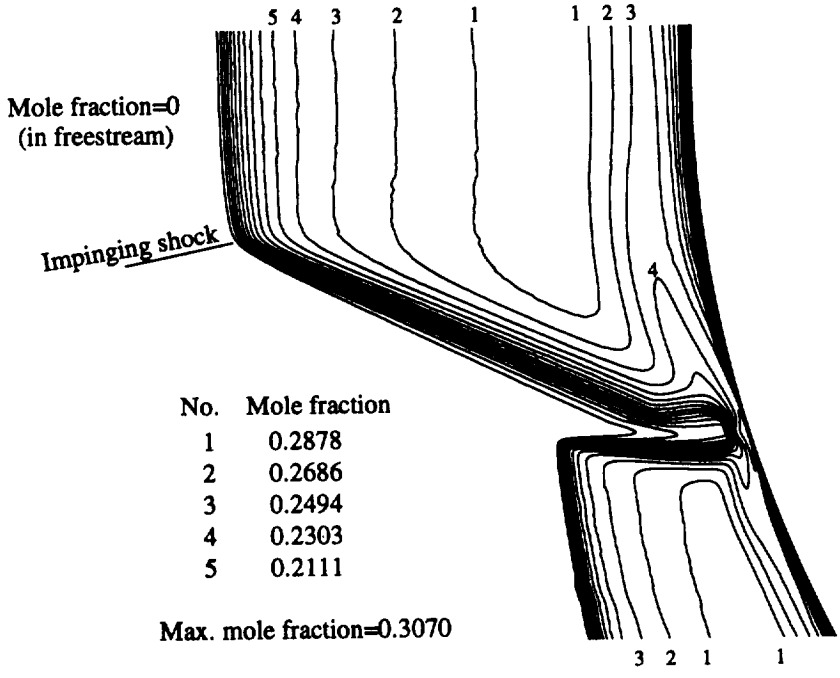

(b) O mole fraction

Figure 12. O2 and O mole fraction contours for Mach 15 shock interference flow; catalytic wall

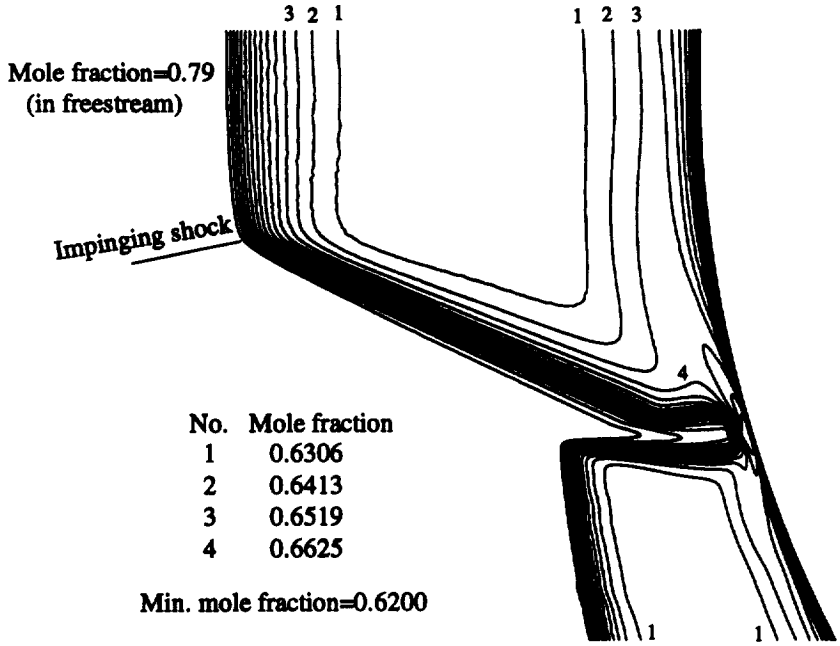

(a) N2 mole fraction

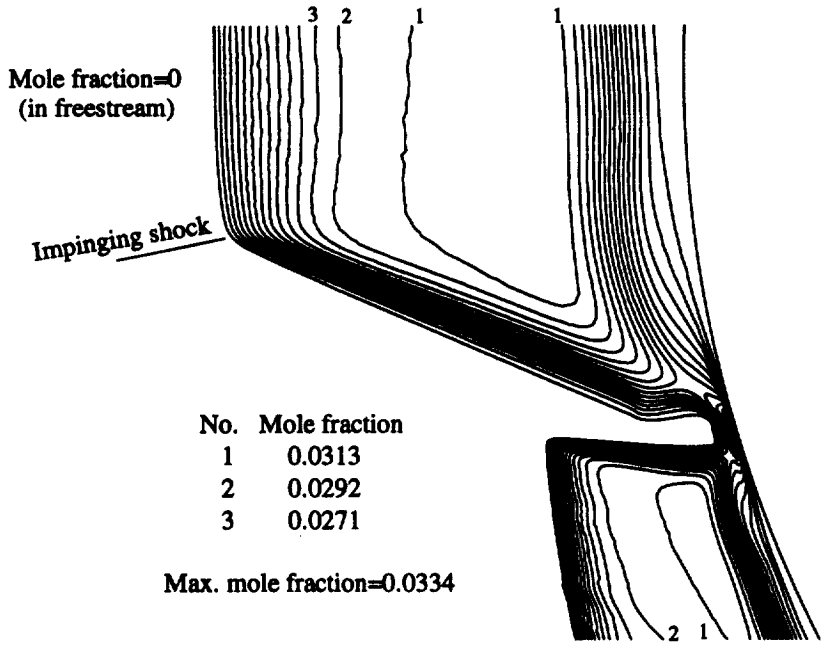

(d) N mole fraction

Figure 13. N2 and N mole fraction contours for Mach 15 shock interference flow; catalytic wall

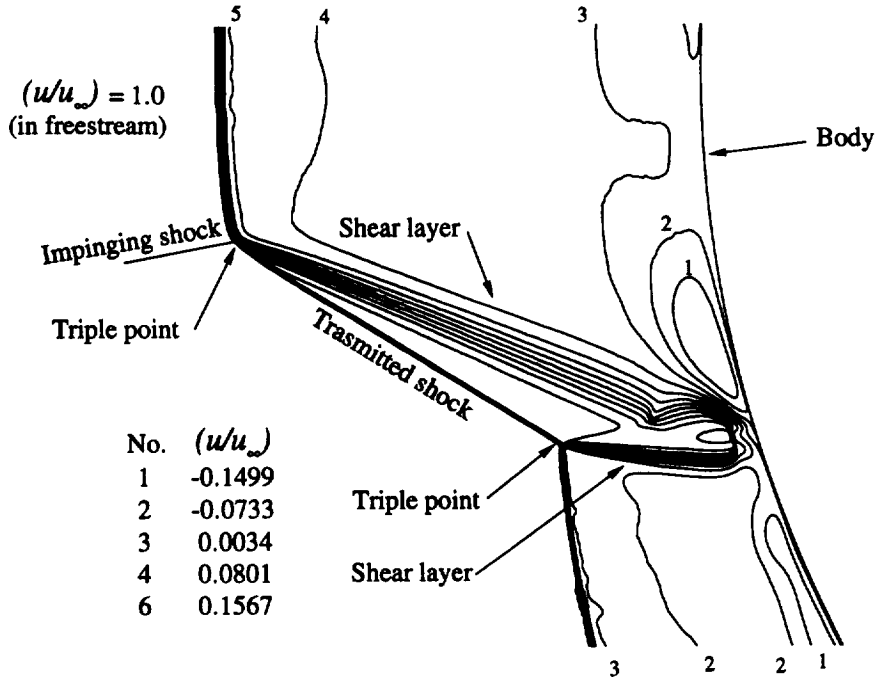

(a) Contours of (u/u_∞)

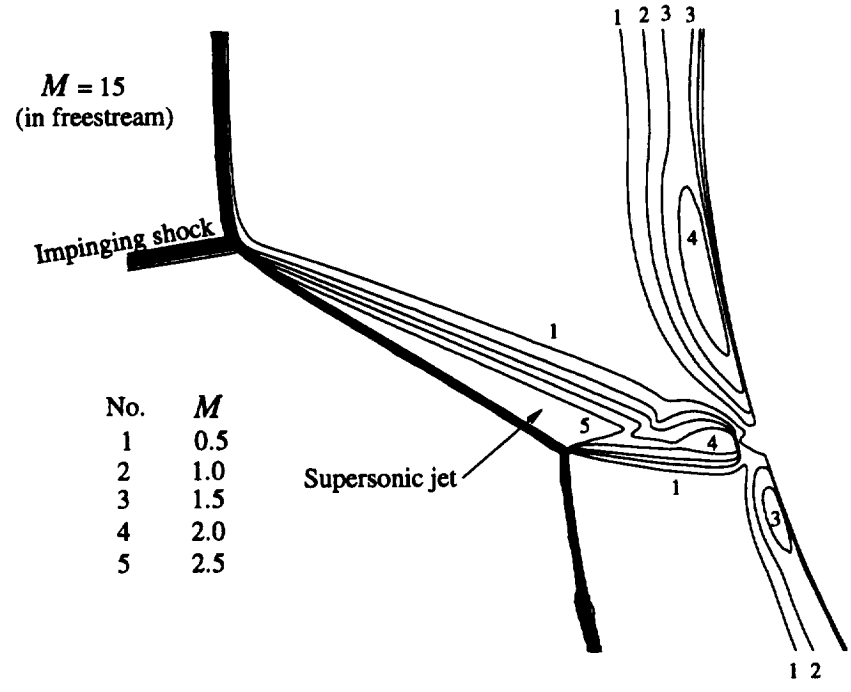

(b) Mach number

Figure 14. Contours of u-velociy and Mach number for Mach 15 shock interference flow; catalytic wall

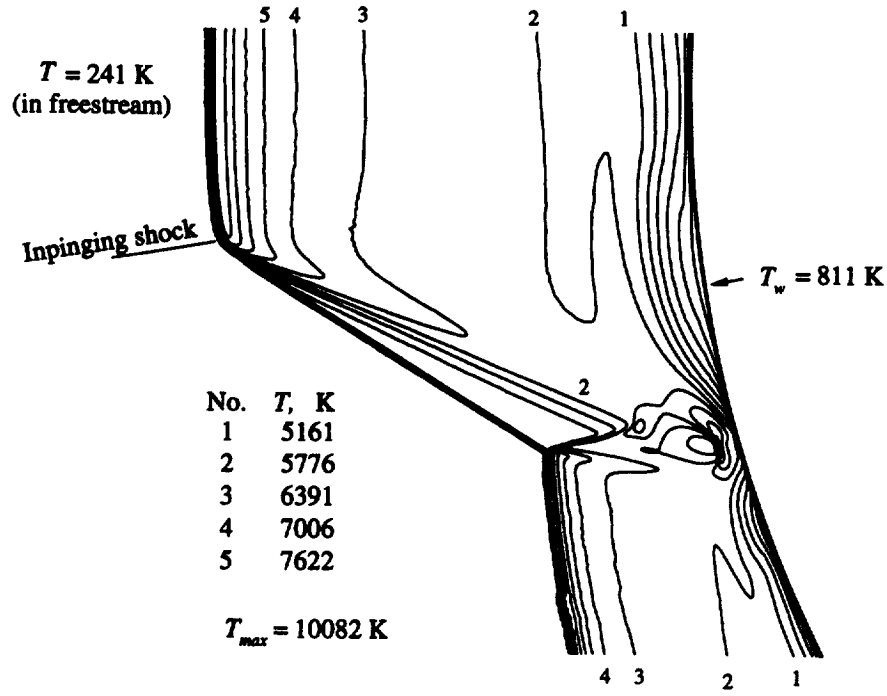

(a) Translational temperature

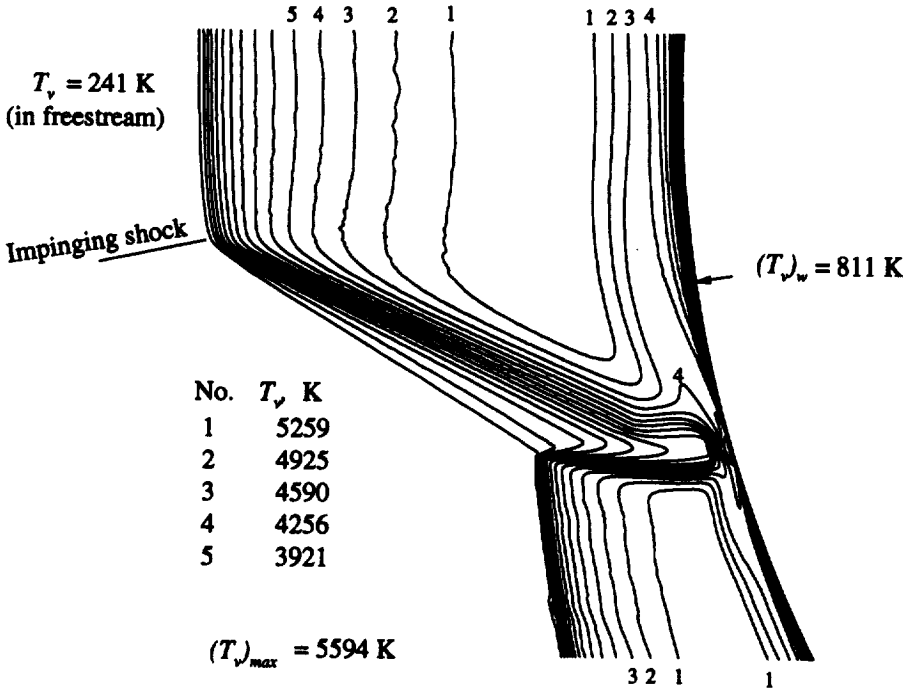

(b) Vibrational temperature

Figure 15. Translational and vibrational temperature contours for Mach 15 shock interference flow; catalytic wall

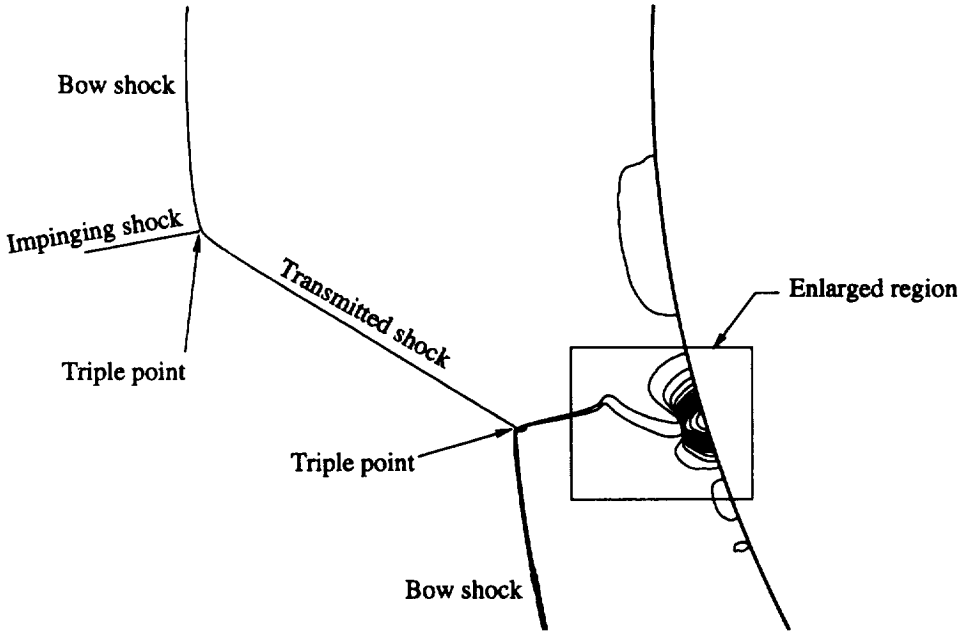

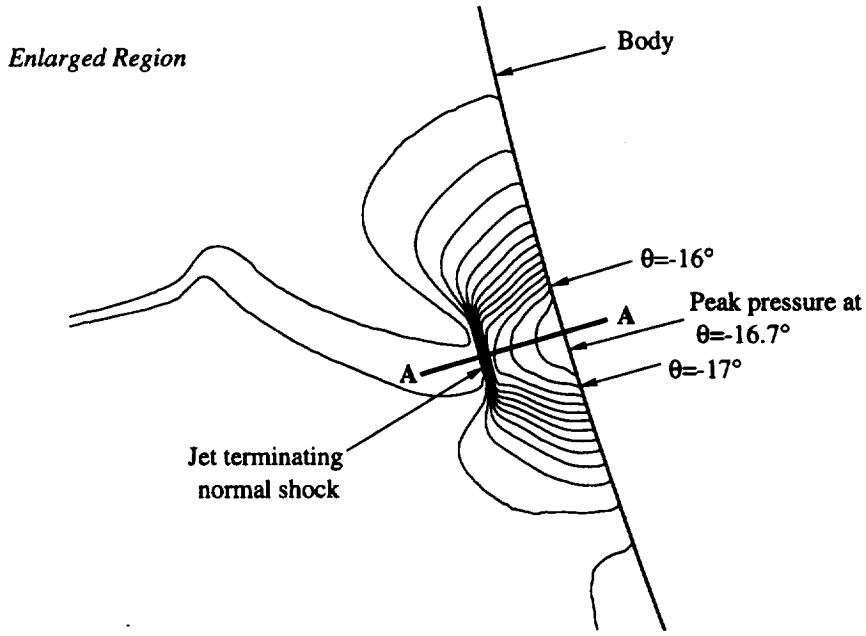

Figure 16. Pressure contours for Mach 15 shock interference flow; fully catalytic wall

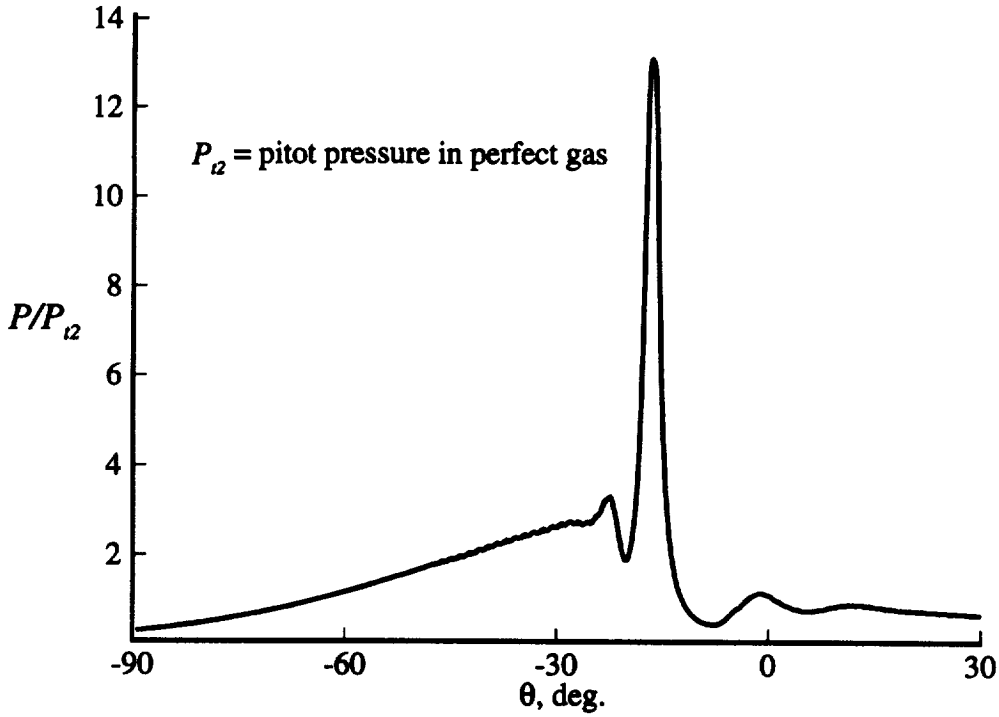

Figure 17a. Pressure distribution on the body for Mach 15 shock interference flow (fully catalytic and noncatalytic walls)

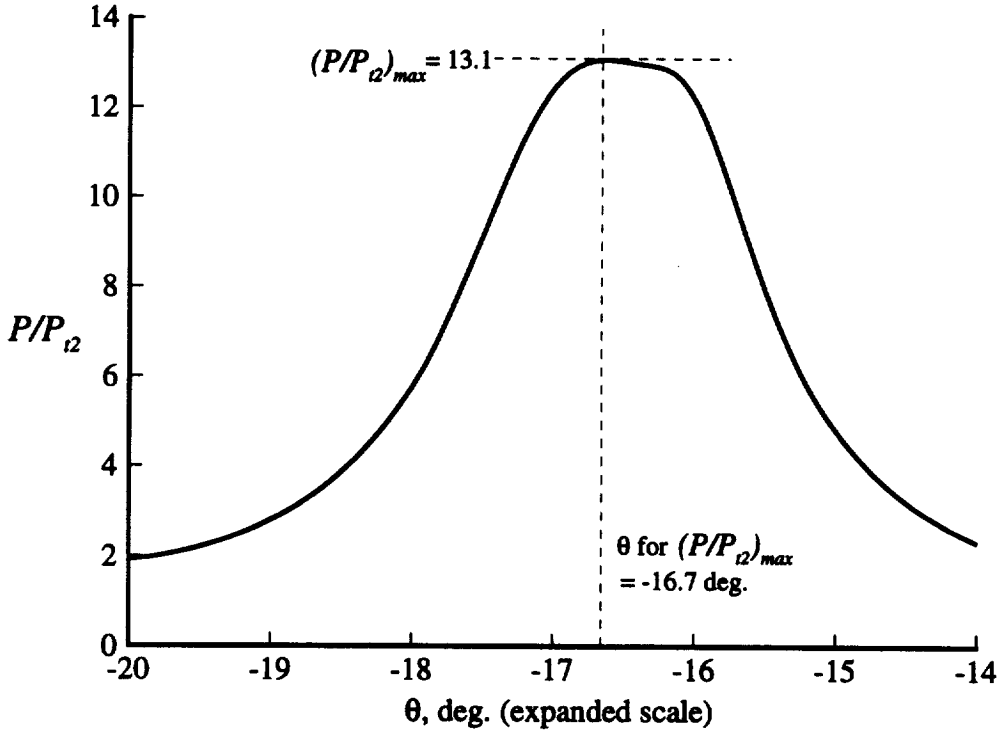

Figure 17b. Pressure distribution near the stagnation point on the body for Mach 15 shock interference flow (fully catalytic and noncatalytic walls)

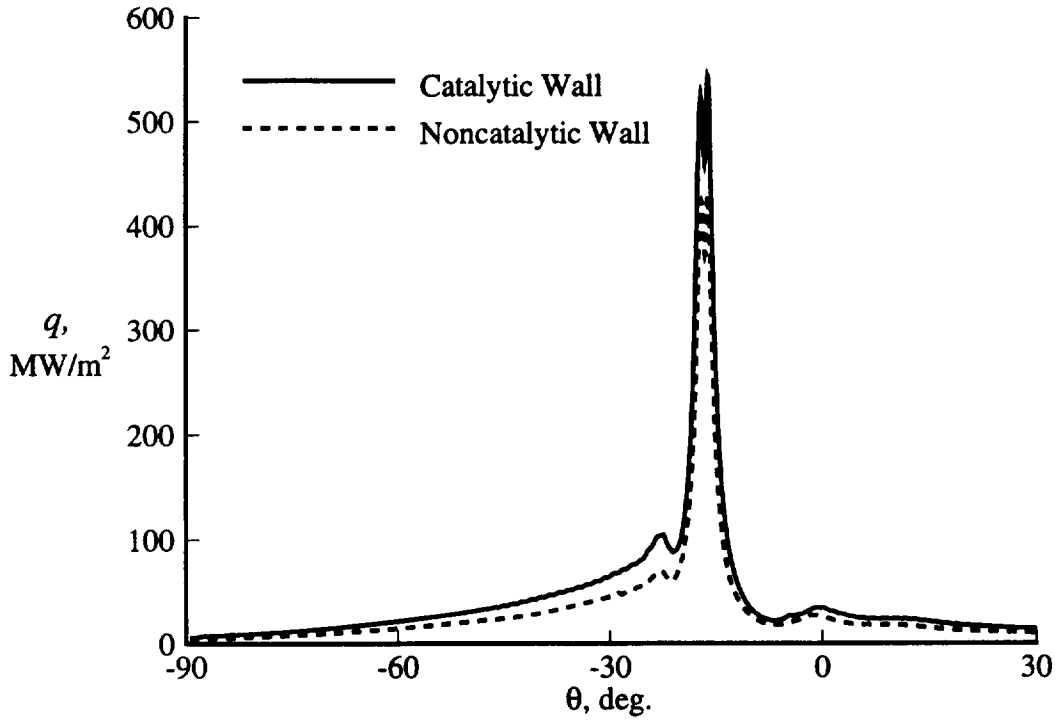

Figure 18a. Heat flux distribution on the body for Mach 15 shock interference flow

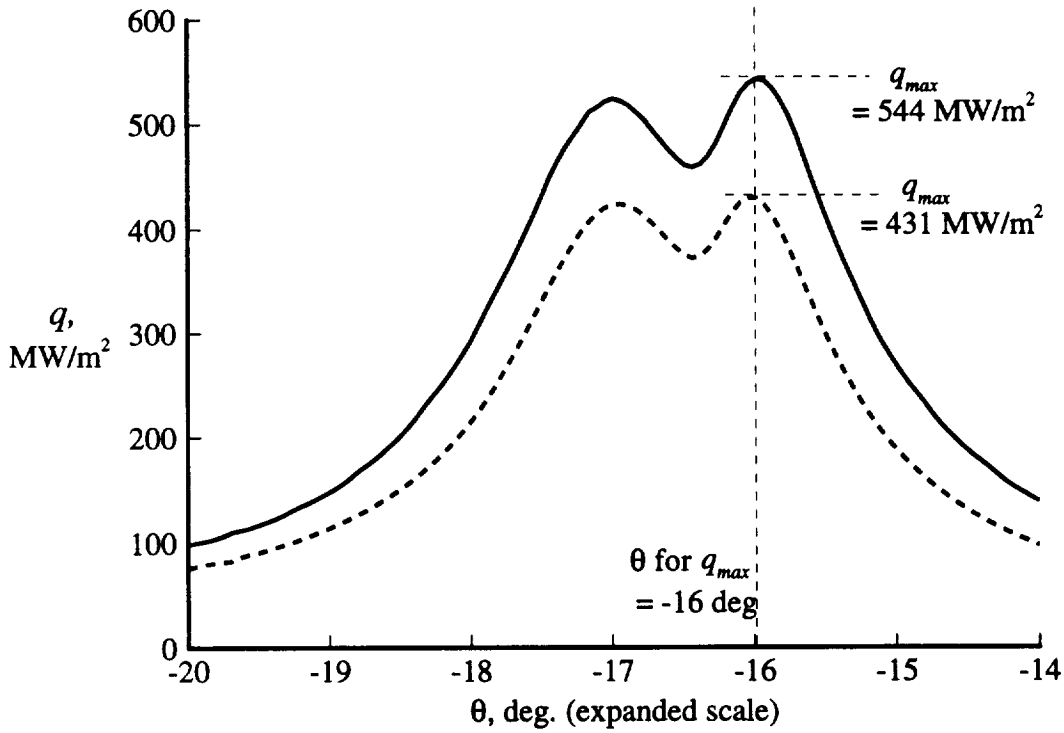

Figure 18b. Heat flux distribution near the stagnation point on the body for Mach 15 shock interference flow

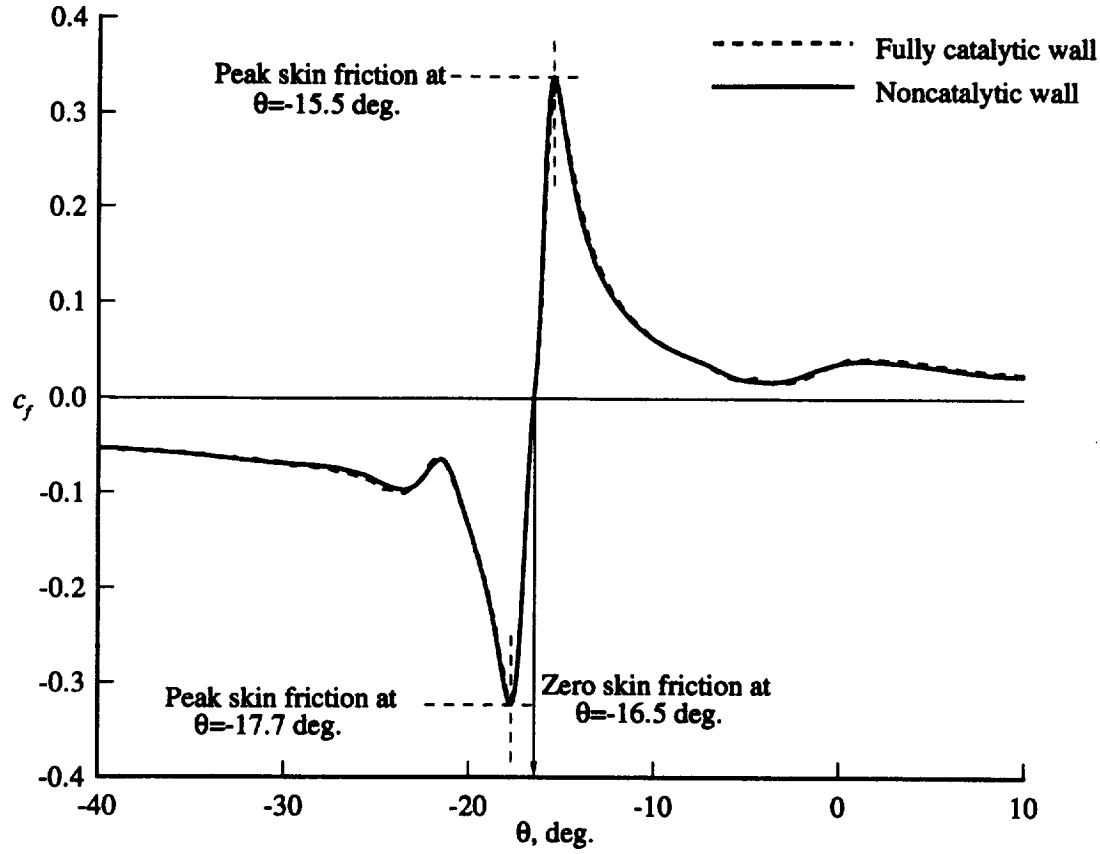

Figure 19. Skin friction distribution of the body for Mach 15 shock interference flow

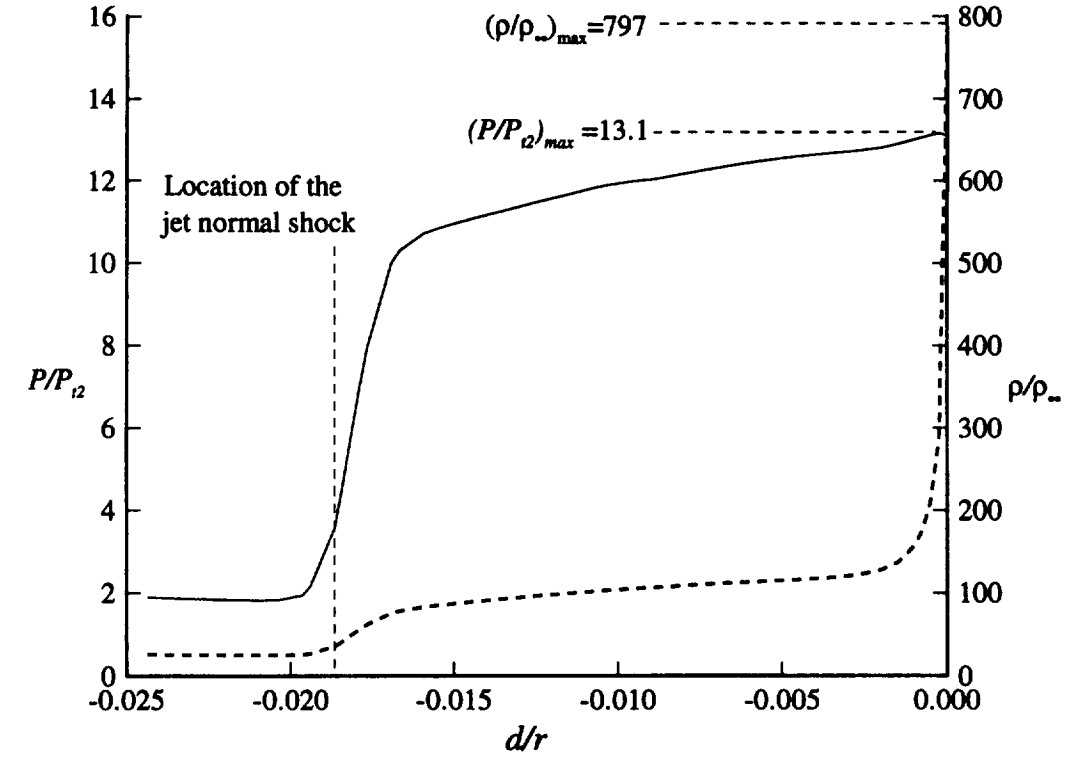

Figure 20a. Pressure and desity distributions along Cut A-A for Mach 15 shock interference flow; noncatalytic wall.

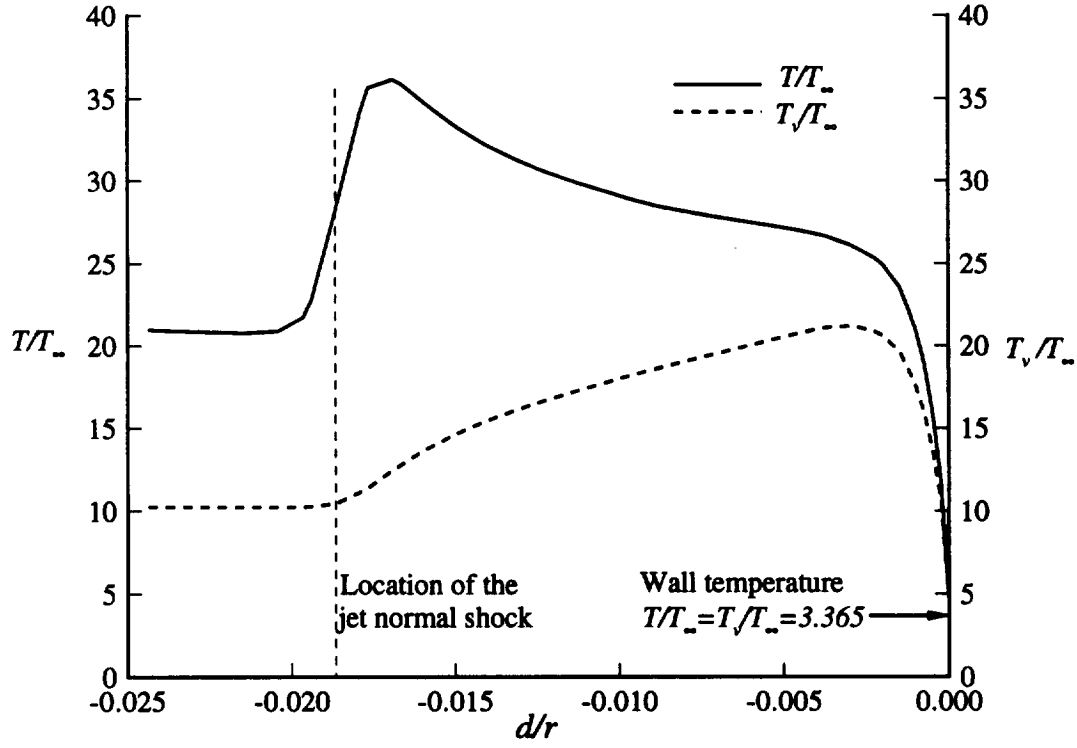

Figure 20b. Translational and vibrational tempertaure distributions along Cut A-A for Mach 15 shock interference flow; noncatalytic wall

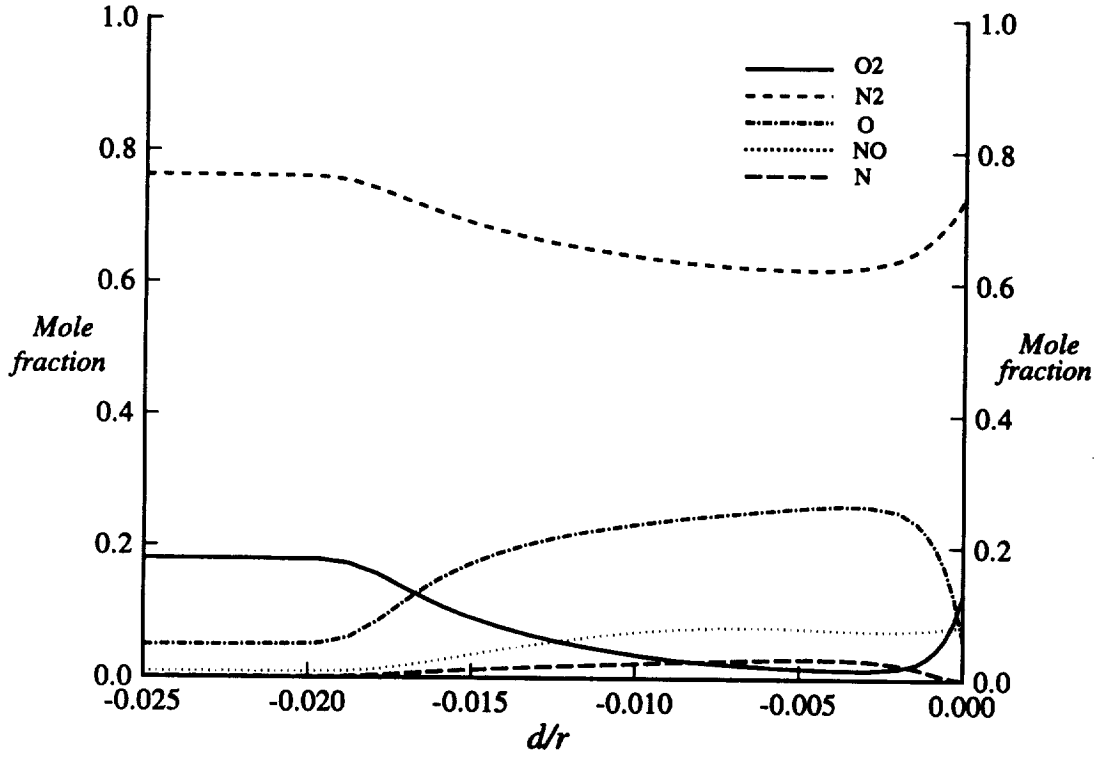

Figure 20c. Mole fraction distributions along Cut A-A for Mach 15 shock interference flow; catalytic wall

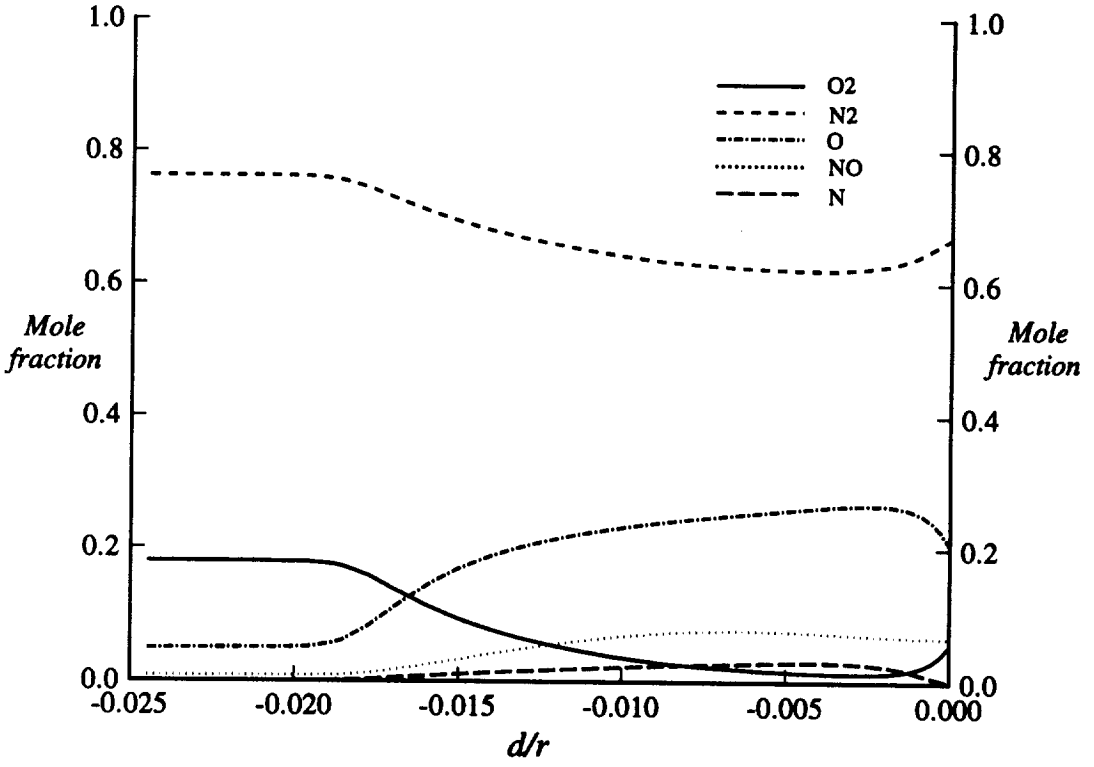

Figure 20d. Mole fraction distributions along Cut A-A for Mach 15 shock interference flow; noncatalytic wall.

REPORT DOCUMENTATION PAGE

Form Approved
OMB No. 0704-0188

1. AGENCY USE ONLY *(Leave blank)*	2. REPORT DATE	3. REPORT TYPE AND DATES COVERED
	August 1994	Contractor Report

4. TITLE AND SUBTITLE
An Implementation of a Chemical and Thermal Nonequilibrium Flow Solver on Unstructured Meshes and Application to Blunt Bodies

5. FUNDING NUMBERS
C NAS1-19000
WU 232-01-04-06

6. AUTHOR(S)
Ramadas K. Prabhu

7. PERFORMING ORGANIZATION NAME(S) AND ADDRESS(ES)
Lockheed Engineering & Sciences Company
Langley Program Office
144 Research Drive
Hampton, VA 23666

8. PERFORMING ORGANIZATION REPORT NUMBER

9. SPONSORING / MONITORING AGENCY NAME(S) AND ADDRESS(ES)
National Aeronautics and Space Administration
Langley Research Center
Hampton, VA 23681-0001

10. SPONSORING / MONITORING AGENCY REPORT NUMBER
NASA CR-194967

11. SUPPLEMENTARY NOTES
Langley Technical Monitor: Allan R. Wieting

12a. DISTRIBUTION / AVAILABILITY STATEMENT
Unclassified - Unlimited
Subject Category 34

12b. DISTRIBUTION CODE

13. ABSTRACT *(Maximum 200 words)*

This paper presents a nonequilibrium flow solver, implementation of the algorithm on unstructured meshes, and application to hypersonic flow past blunt bodies. Air is modeled as a mixture of five chemical species, namely O2,N2,O,NO, and N, and having two temperatures namely translational and vibrational. The solution algorithm is a cell centered, point implicit upwind scheme that employs Roe's flux difference splitting technique. Implementation of this algorithm on unstructured meshes is described. The computer code is applied to solve Mach 15 flow with and without a Type IV shock interference on a cylindrical body of 2.5mm radius representing a cowl lip. Adaptively generated meshes are employed, and the meshes are refined several times until the solution exhibits detailed flow features and surface pressure and heat flux distributions. Effects of a catalytic wall on surface heat flux distribution are studied. For the Mach 15 Type IV shock interference flow, present results showed a peak heat flux of 544 MW/m^2 for a fully catalytic wall and 431 MW/m^2 for a fully catalytic wall. Some of the results are compared with available computational data.

14. SUBJECT TERMS
Hypersonic
Nonequilibrium Flows
Shock Interference Heating

15. NUMBER OF PAGES
51

16. PRICE CODE
A04

17. SECURITY CLASSIFICATION OF REPORT	18. SECURITY CLASSIFICATION OF THIS PAGE	19. SECURITY CLASSIFICATION OF ABSTRACT	20. LIMITATION OF ABSTRACT
Unclassified	Unclassified		